Mon. Not. R. Astron. Soc. **000**, 000–000 (0000) Printed 28 January 2015 (MN LATEX style file v2.2)

Long way to go: how outflows from large galaxies propagate through the hot halo gas

Kartick Chandra Sarkar[1,2] ⋆, Biman B. Nath[1], Prateek Sharma [2], Yuri Shchekinov[3]

[1] *Raman Research Institute, Bangalore, India, 560080*
[2] *Department of Physics & Joint Astronomy Program, Indian Institute of Science, Bangalore, India, 560012*
[3] *Southern Federal University, Rostov-on-Don, Russia*

arXiv:1409.4874v2 [astro-ph.GA] 27 Jan 2015

28 January 2015

ABSTRACT

Using hydrodynamic simulations, we study the mass loss due to supernova-driven outflows from Milky Way type disk galaxies, paying particular attention to the effect of the extended hot halo gas. We find that the total mass loss at inner radii scales roughly linearly with total mass of stars formed, and that the mass loading factor at the virial radius can be several times its value at inner radii because of the swept up hot halo gas. The temperature distribution of the outflowing material in the inner region (∼10 kpc) is bimodal in nature, peaking at 10^5 K and $10^{6.5}$ K, responsible for optical and X-ray emission, respectively. The contribution of cold/warm gas with temperature $\leqslant 10^{5.5}$ K to the outflow rate within 10 kpc is $\approx$ 0.3–0.5. The warm mass loading factor, η_{3e5} ($T \leqslant 3 \times 10^5$ K) is related to the mass loading factor at the virial radius (η_v) as $\eta_v \approx 25\,\eta_{3e5}\left(\mathrm{SFR/M_\odot yr^{-1}}\right)^{-0.15}$ for a baryon fraction of 0.1 and a starburst period of 50 Myr. We also discuss the effect of multiple bursts that are separated by both short and long periods. The outflow speed at the virial radius is close to the sound speed in the hot halo, $\lesssim$ 200 km s^{-1}. We identify two 'sequences' of outflowing cold gas at small scales: a fast ($\approx$ 500 km s^{-1}) sequence, driven by the unshocked free-wind; and a slow sequence ($\approx \pm$100 km s^{-1}) at the conical interface of the superwind and the hot halo.

Key words: Galaxies: mass models – outflow – hydrodynamics – cosmology

1 INTRODUCTION

Galaxies do not evolve as closed systems, and the amount and nature of infall and outflow regulate the crucial aspects of galactic evolution. The movement of gas in and out of a galaxy plays a crucial role in dictating the star formation history of the galaxy, which in turn determines other aspects of its evolution. The infall and outflow of gas also shape the so-called galaxy eco-system, in the immediate vicinity of the galaxy. Not only the evolution of the galaxy itself, but galactic outflows also have cosmological importance because they enrich the intergalactic medium (IGM) with metals. The infall of the IGM gas into a galaxy depends, among other things, on the cooling efficiency of this gas, which in turn depends on the efficiency of outflows in depositing mass and metals. Galactic outflows, and in particular the amount of mass lost, are therefore important links between galactic and cosmological evolution. This requires a detailed study of their dynamics up to the virial radius.

The mass loss rate in outflows has been estimated in various ways in the literature. In the standard scenario, outflows are believed to be excited mostly through the effect of multiple supernovae (SNe) arising from vigorous star formation in a galaxy. Recently other possible mechanisms, such as radiation pressure on dust grains embedded in the outflowing gas, and cosmic rays have also been invoked in launching these outflows. In the SNe driven scenario, Larson (1974) estimated the total mass lost by equating the total thermal energy deposited in the interstellar medium (ISM) by multiple SNe, to the escape energy of the outflowing gas in a galaxy (which depends on the total mass, baryonic mass and the size of the galaxy). Equivalently, the mass lost equals the total thermal

⋆ kcsarkar@rri.res.in

© 0000 RAS

energy of the ISM divided by the square of the wind speed, which is likely of order the sound speed of the hot gas. This led to an estimate that a galaxy of mass (all baryonic) $\sim 5 \times 10^9$ $M_\odot$ would lose half of its mass in an outflow, and larger galaxies would lose relatively less mass. This idea led Dekel & Silk (1986) to consider the effect of such winds in the evolution of dwarf galaxies, and they found that outflows from halos with virial speed less than $\sim$ 100 km s^{-1} have sufficient energy to eject most of the halo gas. This result suggested a dividing line between bright and diffuse dwarf galaxies (see also Babul & Rees (1992)). If the outflow speed is comparable to the escape speed (which scales with the disk rotation speed, v_c), then it also means that the ratio of mass loss rate to SFR $\eta (\equiv \dot{M}/\mathrm{SFR}) \propto v_c^{-2}$ for energy driven outflows. Such estimates of mass (and metals) lost were used in the early, semi-analytical calculations for the enrichment of the IGM (Tegmark & Silk 1993; Nath & Trentham 1997; Ferrara et al. 2000a). If other mechanisms such as radiation pressure should dominate, then it has been shown that the outflow would be momentum driven instead of being driven by energy, and that $\eta \propto v_c^{-1}$ (Murray et al. 2005).

However, as observations of typical multiphase outflows (such as in M82) suggest, the estimate of mass lost is likely to be more complicated than as outlined above. The outflowing material consists of gas at different temperatures (ranging from the X-ray emitting hot gas to a cold phase containing molecular gas), and the speed throughout the outflow is hardly uniform. The multiphase temperature/density structure and dynamics is further complicated by the non-spherical morphology of the outflow, which is moulded into a biconical shape by the interaction with the stratified disk material of the star forming galaxy.

The multidimensional and multiphase nature of galactic outflows calls for a more detailed numerical modelling, especially because only certain phases at smaller scales are accessible to observations. For the IGM, however, the scales close to the virial radius are the most important. Therefore, it is essential to understand the relation between outflows at various scales via controlled numerical simulations.

Numerical simulations have helped one to overcome the limitations of 1-D semi-analytical calculations. Mac Low & Ferrara (1999) simulated SNe driven superbubbles of various mechanical luminosities in disks embedded in dark matter halos, and determined their efficiency in driving outflows from low-mass galaxies. The central source of energy (and mass) injection had a constant luminosity maintained for 50 million years. They found the range of luminosities (related to the star formation rate) that can drive out gas, completely or partially, from galaxies of different masses. They found that only a small fraction of the total gas mass was expelled, except in the smallest galaxy considered (with 10^6 $M_\odot$ gas). However, because of the absence of the hot halo gas in their simulations, the results cannot be directly applied to higher mass galaxies ($M \gtrsim 10^{12}\, M_\odot$). The hot gas density in the halo is expected to be non-negligible, $n \sim 10^{-4}$ cm^{-3} (e.g., see Sharma et al. 2012), for a Milky-Way mass galaxy, and therefore the halo gas must be included in order to study outflows at scales > 10 kpc.

Recent simulations with GADGET (which includes the halo gas) by Hopkins et al. (2012) have compared the efficiency of different physical processes in driving outflows, and also determined some scaling relations for the mass lost as a function of the galactic mass and disk column density. However, these simulations study the outflow within a region of 50 kpc, and cannot be treated as an estimate of mass outflow at the virial radius. Moreover, in these simulations (unlike that of Mac Low & Ferrara (1999)), the outflows are linked to the SFR, which is in turn linked to the disk gas density, and which ultimately depends on the galaxy mass. It is crucial to understand the dependence of the large scale outflows on the halo mass and the SFR, since cosmological simulations of IGM enrichment that are not capable of resolving galaxies, rely on such prescriptions. E.g., Oppenheimer et al. (2006) used various scaling for the mass loading factor (η, the ratio of mass loss rate to the SFR) with the galactic mass or velocity dispersion of the halo ($\eta \propto \sigma^{-1}, \sigma^{-2}$) in order to match the simulation results with observations.

The mass loading factor estimated at the virial radius has important implications for understanding dynamical processes accompanying enrichment of the Universe. Recent observations of the extended circum-galactic haloes bearing metals up to distances 100 – 200 kpc from the parent galaxy (Tumlinson et al. 2011; Bordoloi et al. 2014; Mathes et al. 2014) call for a long-term numerical study covering passage of the outflows through the virial threshold.

Hopkins et al. (2012) also found that the outflowing gas is mostly dominated by warm gas ($10^4 < T < 4 \times 10^5$ K), which is consistent with the results of Melioli et al. (2013) who have simulated the outflow from M82. However, it would be important to know the mass distribution of gas at different temperatures as a function of SFR and galactic mass, and at different galacto-centric radii. This is needed to compare the theoretical/simulation results with observations which are limited to small distances. For example, Martin (1999) found that the rate of mass loss in the form of gas at $\sim$ 1 keV is comparable to the SFR for galaxies with low rotation speed ($\leqslant$ 130 km s^{-1}). However, these estimates are relevant for small distances (typically $\sim$ 0.1 of the virial radius) where the emission measure of the gas is large, and may not be useful if one considers the mass flux at the virial radius, which is required for studies of the enrichment of the IGM.

Observationally, the estimates of the mass loading factor η has focussed on L_* galaxies at $z \leqslant 1$, with stellar masses of a few times 10^{10} $M_\odot$. These estimates range between $\eta \sim 0.3$–30 in this galactic mass range for $z \sim 0.1$ (Rupke & Veilleux 2013; Heckman et al. 2000; Bouché et al. 2012; Bolatto et al. 2013). At high redshifts, the estimates appear to be similar to values at present epoch (Martin et al. 2012; Newman et al. 2012). The corresponding observed outflow speed ranges between 100–800 km s^{-1}. In a semi-analytic calculation, Lagos et al. (2013) has predicted that η saturates below a circular velocity of $\sim$ 80 km s^{-1}. However, their calculation is limited

to 1-D dynamics and also to length scales of order the disk height.

In this paper we investigate outflow properties varying the star formation rate over a wide range, keeping the ISM and halo properties fixed to the Milky Way values. Our study is similar in spirit to that of Mac Low & Ferrara (1999), but we include the effect of hot halo gas in constraining the outflowing gas. We do not consider the effects of mass loading on the central conical outflow from thermally evaporated clumps and pre-existing clouds in the ISM (before the launch of the outflow), as in Suchkov et al. (1996). We have also investigated the relation between outflows in the cold phase and the total outflow rate at smaller scales and at the virial radius. Moreover, we investigate the detailed kinematics of the cold/warm gas and relate it with observations.

The paper is organised as follows. In §2, we discuss the mass model of the simulated galaxy, setting an equilibrium initial condition and selection of the injection parameters. In §3, we describe the PLUTO simulation code and various settings that we use. In §4, we present the results of our runs, in §5, we discuss some of the implications of our work and finally in §6 we summarise our key findings.

2 MASS MODEL OF THE GALAXY

2.1 Gravitational potentials

To model the density distribution of the gas , we consider two gravitational potentials. For the disk, we use the Miyamoto & Nagai potential (Miyamoto et al. 1975) (in cylindrical coordinates (R, z)),

$$\Phi_{\rm disk}(R,z) = -\frac{GM_{\rm disk}}{\sqrt{R^2 + (a + \sqrt{z^2+b^2})^2)}}, \quad (a, b \geqslant 0) \qquad (1)$$

where a and b represent the scale length and the scale height of the disk (mass $M_{\rm disk}$) respectively. For the dark matter, we use a modified form of the NFW dark matter (DM), which unlike the original NFW profile (Navarro et al. 1996), has a core with a finite dark matter density at the centre. The potential is given as

$$\Phi_{\rm DM} = -\left(\frac{GM_{\rm vir}}{f(c)\, r_s}\right) \frac{\log(1+\sqrt{R^2+z^2+d^2}/r_s)}{\sqrt{R^2+z^2+d^2}/r_s} \quad (d \geqslant 0), \qquad (2)$$

where $f(c) = \log(1+c) - c/(1+c)$ with $c = r_{\rm vir}/r_s$, the concentration parameter and d is the core radius of the DM distribution (see appendix B for the DM density profile). $M_{\rm vir}$, $r_{\rm vir}$ and r_s are the total mass of the galaxy (including DM), the virial radius and scale radius respectively. A full list of parameters for the model galaxy is given in the Table 1.

2.2 Setting the initial density distribution

In our model, we consider two components of the interstellar medium (ISM): warm ionised medium (WIM), and a hot ionised medium (HIM). Since the WIM (T $\sim 10^4$K, hereafter we call it the disk gas) is a part of the disk gas which is rotating along with the stars, we consider the effect of rotation on the density distribution of the WIM. The HIM, however, according to the galaxy formation theory, traces out the potential of the dark matter with no net rotation and has a temperature close to the virial temperature of the halo ($T_{\rm halo} \sim 3\times10^6$K for MW type galaxy). This prescription is similar to the set-up of Suchkov et al. (1994).

To construct the initial density distribution for the combined gas, we consider the Euler's equation in steady state

$$-\frac{\nabla p}{\rho} - \nabla\left(\Phi_{\rm DM} + \Phi_{\rm disk}\right) + \frac{v_{\phi,g}^2}{R}\hat{R} = 0\,, \qquad (3)$$

for each of the components. Here, p is pressure, ρ is density and $v_{\phi,g}$ is the gas rotation velocity. Since for the gas in the disk , the gravitational force is balanced by rotation and gas

parameters	values
$M_{\rm vir}(\rm M_\odot)$	10^{12}
$M_{\rm disk}(\rm M_\odot)$	5×10^{10}
$T_{\rm vir}$ K	3×10^6
$r_{\rm vir}$ (kpc)	258
c	12
r_s (kpc)	21.5
a (kpc)	4.0
b (kpc)	0.4
d (kpc)	6.0
$c_{s,\sigma}$ (km s^{-1})	20.8
$\mathcal{Z}_{\rm disk}$ ($\mathcal{Z}_\odot$)	1.0
$\mathcal{Z}_{\rm halo}$ ($\mathcal{Z}_\odot$)	0.1
$\rho_c(0,0)$ ($\rm m_p cm^{-3}$)	3.0
H_R (kpc)	~ 2.2
H_z (kpc)	$\simeq 0.2$
$M_{\rm WIM}(\rm M_\odot)$	7×10^8
$\rho_{\rm hot}(0,0)$ ($\rm m_p cm^{-3}$)	1.1×10^{-3}

Table 1. Parameters used in our simulations.

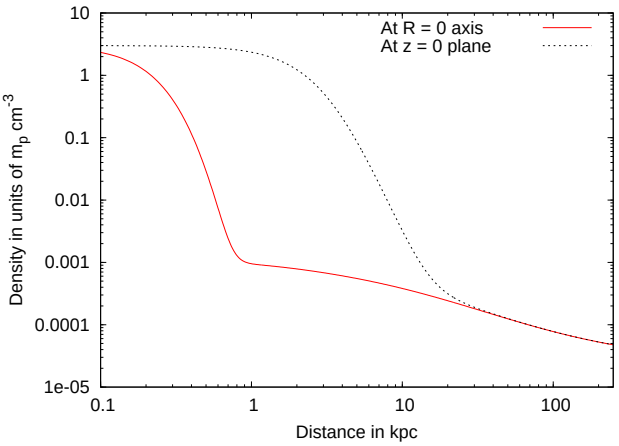

Figure 1. Gas density profiles for the model galaxy along R and z. It shows that the disk component dominates at smaller R and z, and at larger distances, the halo component dominates.

pressure together, the rotation speed is less than the particle rotation velocity, $v_{\phi,G} = \sqrt{R\left[\frac{\partial\Phi}{\partial R}\right]_{z=0}}$, which is solely determined by gravity. For simplicity, we take the rotation velocity of the gas as a fraction (f = constant, chosen to be 0.95) of $v_{\phi,G}$ at that point: $v_{\phi,g} = f v_{\phi,G}$. Therefore, the density distribution for the warm disk gas can be written as,

$$\rho_d(R,z) = \rho_c(0,0)\,\exp\Big(-\frac{1}{c_{\rm sc}^2}[\Phi(R,z)-\Phi(0,0) - f^2(\Phi(R,0)-\Phi(0,0))]\Big)\,, \quad (4)$$

and for the hot halo gas,

$$\rho_h(R,z) = \rho_h(0,0)\,\exp\left(-\frac{1}{c_{\rm sh}^2}\left[\Phi(R,z)-\Phi(0,0)\right]\right)\,, \quad (5)$$

where, $\rho_c(0,0)$ and $\rho_h(0,0)$ are the warm and hot central densities and $c_{\rm sc}$ and $c_{\rm sh}$ are the isothermal sound speeds of the warm disk and hot halo, respectively (more details on the set-up are given in appendix C). In Figure 1 we show the steady state gas density distribution along the minor axis (red solid line) and the major axis (black dotted line). This figure shows that each profile consists of two features, one high density structure at lower radii representing the disk material, and another, low density and comparatively flatter distribution at larger radii representing the halo gas.

In disk galaxies, along with the thermal pressure, there is pressure due to turbulence, magnetic fields and cosmic rays, which arises because of the continuous stirring of gas by supernovae. Therefore, the dynamics of the disk is determined by both thermal and non-thermal pressures, for which the effective sound speed can be written as

$$c_{s,\rm eff}^2 = c_{s,T}^2 + c_{s,\sigma}^2\,, \quad (6)$$

where, $c_{s,T}$ is the isothermal sound speed corresponding to a temperature T and $c_{s,\sigma}$ is the effective sound speed due to non-thermal components. We include these effects by assuming a disk temperature of 4×10^4 K, with an effective sound speed $c_{s,\rm eff} = 24$ km s^{-1} (larger than $c_{s,T}$, the sound speed of WIM at 10^4 K).

For the disk , we set the central density to be 3.0 particles per cm^3. The hot halo is however less constrained by observations. In order to fix the central density of the hot halo, we normalise the halo mass distribution to give a total halo gas mass $M_{h,\rm gas} = 0.11 M_{\rm vir}$ and ratio of the stellar disk mass to the virial mass $M_{\rm vir}$ is 0.05, as in the scenario of Mo, Mao and White (1998). Thus, the halo has a global baryon fraction of 0.16, consistent with the cosmic value of $f_b = \Omega_b/\Omega_m$. Some of the recent observations have revealed that the baryon fraction can be ~ 0.1 for massive spirals (Bogdan et al. 2013), and in our MW, this fraction can be ~ 0.16 for a gas with polytropic index $\gamma = 5/3$ in hydrostatic equilibrium (Fang et al. 2013; Gatto et al. 2013). Though here we assume $f_b = 0.16$, we have also checked the effect of f_b on the mass loading factor at virial radius (see §4.3).

The total density is the sum of the densities of the hot halo and warm disk components, $\rho = \rho_d + \rho_h$. Since the halo gas does not rotate, the effective rotation speed $v_{\phi,\rm net}$ for the combined gas is given as

$$\rho v_{\phi,\rm net}^2 = \rho_d\, v_{\phi,g}^2\,, \quad \Rightarrow \quad v_{\phi,\rm net} = f\sqrt{\frac{\rho_d}{\rho}R\left[\frac{\partial\Phi}{\partial R}\right]_{z=0}}\,. \quad (7)$$

We have found that the above prescription for the initial set up is remarkably stable over a time scale of 1 Gyr. In reality (in 3D), the interaction between the non-rotating halo gas and the rotating disk gas could generate instabilities. We can estimate the time scale for Kelvin-Helmholtz instability at the interface of the rotating disk and the non-rotating halo. The dominant wavelength of perturbation is ~ 10 kpc, the corresponding relative velocity ~ 100 km s^{-1}, and the ratio of densities of two gases is ~ 100 (for gases with temperature 10^4 and 10^6 K and in pressure equilibrium). The time scale for the growth of perturbations is therefore ~ 1 Gyr. We have also checked with a 3D simulation run that this steady state holds up to ~ 1 Gyr. Therefore the set up described above is adequate for our simulations.

3 SIMULATION SET-UP

In this section we describe various simulations that we carry out and the numerical setup. We have carried out two kinds of simulations to study galactic outflows: small-scale, short-duration (50 Myr) simulations going out to 30 kpc to focus on the inner regions where most observational constraints come from; and large-scale, longer-duration (1 Gyr) simulations going out to 250 kpc to study cosmological impact of galactic outflows. In cases where we focus on observations of multiphase outflows we use the high-resolution small-scale runs (c.f. Figs. 2, 3, 10, 14, 15, & 16). The large-scale runs are used to infer outflow properties at the halo scale (c.f. Figs. 4, 5, 6, 12, & 13).

We have studied mechanical luminosities ranging from $10^{40.3}$ to 10^{43} erg s^{-1} keeping the model parameters fixed. We have chosen a fiducial run corresponding to a mechanical luminosity injection of $\mathcal{L} = 10^{42}$ erg s^{-1} or SFR = 14.3 M$_\odot$ yr^{-1} (see §3.1), lying in the intermediate regime of luminosities that we have explored. A full list of runs is given in Table 2.

3.1 Injection parameters

In this paper we only focus on supernovae (SNe) driven outflows. Since a single supernova, or even a large number of SNe, is not energetic enough to launch an outflow on larger scales unless they are coherent in space and time (Nath & Shchekinov 2013; Vasiliev et al. 2014), we consider the effect of multiple SNe from a large OB association in the central region of the galaxy. We consider a constant energy input of mechanical luminosity $\mathcal{L}$ from the SNe confined in a spherical region of radius $r_{\rm inj}$ at the centre of the galaxy. We deposit thermal energy to the gas within $r_{\rm inj}$. Sharma et al. (2014) have shown that for such an implementation to work, the injection radius ($r_{\rm inj}$) should be such that the energy deposition time is shorter than the cooling time, and we have adjusted

Name	$r_{\rm max}$ (kpc)	$\mathcal{L}$ (erg s^{-1})	$t_{\rm inj}$ (Myr)	cooling
L1	250	$10^{40.3}$	50	on
L2	250	10^{41}	50	on
L3*	250	10^{42}	50	on
L4	250	10^{43}	50	on
L5	350	$10^{41.3}$	RSB	on
L6	250	$10^{41.7}$	50	on
L7	250	$10^{42.3}$	50	on
L8	250	$10^{42.6}$	50	on
L9	250	10^{42}	25	on
L10	250	10^{42}	100	on
L11	250	10^{42}	200	on
L12	250	10^{42}	25	off
L13	250	10^{42}	50	off
L14	250	10^{42}	100	off
L15	250	10^{42}	200	off
S1	30	$10^{40.3}$	50	on
S2	30	10^{41}	50	on
S3*	30	10^{42}	50	on
S4	30	10^{43}	50	on

Table 2. List of runs: The L-series and S-series represents the large-scale and small-scale simulations respectively. The corresponding box size is given in 2nd column, where $r_{\rm max}$ gives the maximum extent of grid in radial direction. The 3rd and 4th column provides the mechanical luminosity and the injection time of the runs, while the 5th column gives the information about cooling. For L5, RSB means Repeated Star Bursts. The fiducial runs are denoted by an "$*$". Other than these runs, we have also run some simulations with variable baryon fraction (f_b).

our $r_{\rm inj}$ (= 60 pc) according to this constraint. We also assume that each SN releases an energy of 10^{51} ergs, and for a Salpeter mass function, on average, $\dot{M}_{\rm inj} = 0.1\times$ SFR of mass is injected into the interstellar medium (ISM). Therefore, the relation between the mechanical luminosity and SFR can be written as

$$\mathcal{L} = 10^{51} \times \epsilon \times f_{\rm SN} \times {\rm SFR\ erg\ s^{-1}}\,, \tag{8}$$

where, $f_{\rm SN}$ is the number of supernovae explosions per unit mass of stars formed, and ϵ is the efficiency of heating the gas. We assume $\epsilon = 0.3$, consistent with observations (Stickland & Heckman 2007) and theoretical estimates from numerical simulations (Vasiliev et al. 2014). For Salpeter IMF, $f_{\rm SN} = 7.4\times10^{-3}\,/M_\odot$ for lower and upper limits of stars at 0.1 and 100 $M_\odot$. This gives,

$$\mathcal{L} = 7\times10^{40}\ {\rm erg\ s^{-1}}\ \frac{\rm SFR}{(1\,M_\odot\ {\rm yr^{-1}})}\,. \tag{9}$$

This in turn gives the relation between luminosity ($\mathcal{L}$) and the rate of mass injection as

$$\dot{M}_{\rm inj} = 0.014 \times \frac{\mathcal{L}}{10^{40}{\rm erg\ s^{-1}}}\ M_\odot\,{\rm yr^{-1}}\,. \tag{10}$$

The duration of mass and energy injection is assumed to be 50 Myr, the typical lifetime of an OB association. The effect of different star burst duration is are also discussed in §4.2.

3.2 The code settings

We use the publicly available hydrodynamic code PLUTO (Mignone et al. 2007) for our simulations. We run our simulations in 2D (r,θ) spherical coordinates, assuming axisymmetry ($\partial/\partial\phi = 0$). However, we do allow for a non-zero azimuthal velocity v_ϕ. To solve the hydrodynamic equations (Euler equations with numerical dissipation and with mass and energy source terms which drive the outflows), we use piecewise parabolic reconstruction of the primitive variables. We use the advection upstream splitting method (AUSM+; Liou 1996) as the Riemann solver and a third-order Runge-Kutta scheme (RK3) to advance the solution in time.

- *Grid :* Since we inject the SNe energy and mass in a small region of space (= 60 pc) at the centre of the galaxy and try to observe the effects near the virial radius ($\sim$ 250 kpc), we use a logarithmic grid in the radial (r) direction. It starts from 20pc and goes till 250 kpc for the large scale simulations and till 30 kpc for the small-scale simulations. A uniform grid is used in the θ direction going from $\theta = 0$ to $\pi/2$. [1]. For the results mentioned in this paper, we use 512 grid points along both r and θ directions. We have also carried out resolution studies with double and half this resolution in each direction.
- *Boundary conditions :* The inner and outer radial boundary values for mass and energy densities are set to their equilibrium values at $t = 0$ (as discussed in §2.2). The velocities are copied in the radial ghost zones from the nearest active zones. The θ boundary conditions are set as reflective.
- *Metallicity:* Since the mixing of metals at kpc range in ISM densities and temperatures is dominated by the dynamical evolution of the gas rather than diffusion, we track the metallicity by treating it as a passive scaler which follows the simple advection equation. We set the disk metallicity to be equal to the solar metallicity ($\mathcal{Z}_\odot$) and the halo metallicity to be $0.1\,\mathcal{Z}_\odot$.
- *Cooling :* PLUTO can include optically thin losses in a fractional step formalism[1]. It has several different cooling modules, among which, we use the tabulated cooling method which solves the internal energy equation from a given $T - \Lambda(T)$ table. We include the metallicity effect in the cooling rate by using linear interpolation of the cooling curves corresponding to $\mathcal{Z} = \mathcal{Z}_\odot$ and $\mathcal{Z} = 0.1\mathcal{Z}_\odot$ (Sutherland & Dopita 1993), to all other metallicities from $\mathcal{Z}_\odot$ to $0.1\mathcal{Z}_\odot$.

In our calculation, we express the temperature as $T = p/\rho$, which includes the dynamical pressure in addition to the thermal pressure, and therefore the effective temperature of the gas in the disk becomes large enough to induce strong cooling, unlike in the WIM at 10^4 K. To stop this cooling, we constrain the cooling function of the disk material (but not the injected material) to be zero within a box of size $R\times z = 15\times2$ kpc^2, This can be thought of as a crude model of continuous SNe/stellar heating or turbulent support of gas in the disk, which prevents disk cooling.

[1] More can be found in the user's guide of PLUTO - http://plutocode.ph.unito.it/Documentation.html

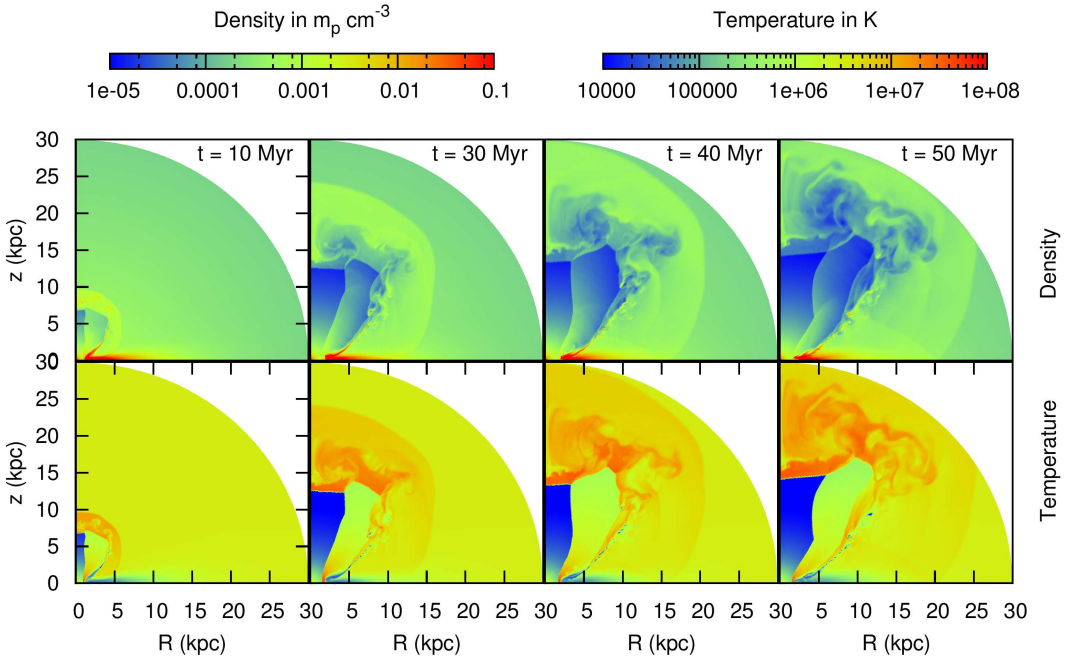

Figure 2. Snapshots of density (top panel) and temperature (bottom panel) at 10, 30, 40 and 50 Myr for $\mathcal{L} = 10^{42}$ erg s^{-1} for a box size of $r_{\rm max} = 30$ kpc. Notice that the cold, multiphase gas, which is mainly due to the uplifted disc gas, is confined to the outer wall of the outflow.

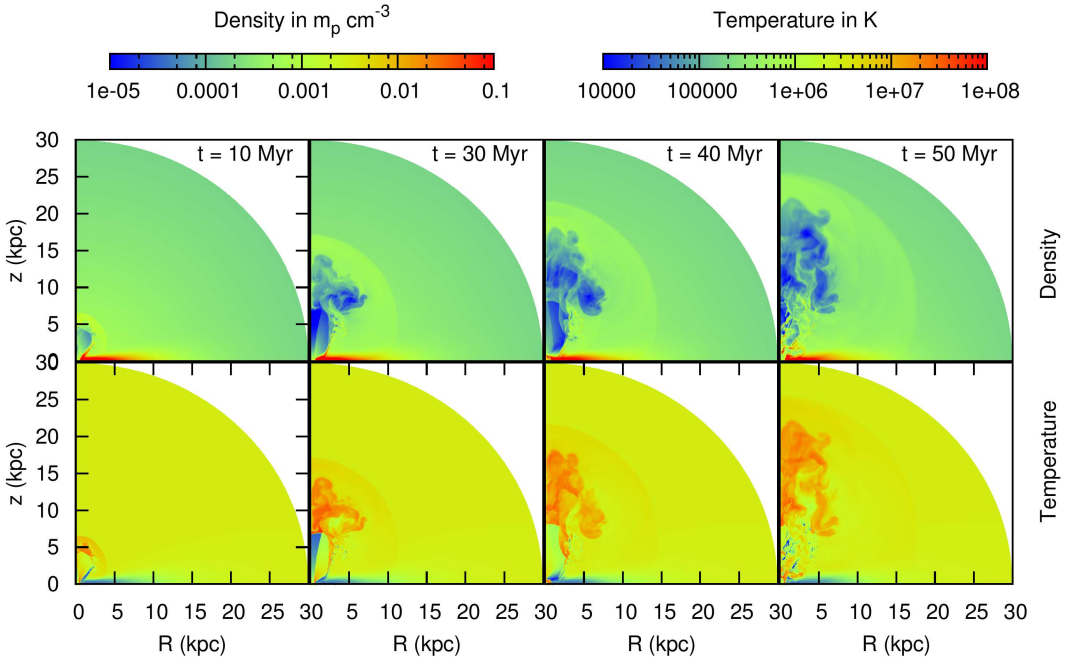

Figure 3. Snapshots of density (top panel) and temperature (bottom panel) at 10, 30, 40 and 50 Myr for $\mathcal{L} = 10^{41}$ erg s^{-1} for a box size of $r_{\rm max} = 30$ kpc. The evolution is different from Figure 2 in that, in addition to the cold gas at the outer wall, there is volume-filling cold disk gas at 50 Myr dredged up by the ram pressure of the outflow. It will be shown later in §4.4 that the cold gas at the outer wall is slower compared to the volume-filling cold gas.

• *Units :* To avoid the calculation of very small ($\sim 10^{-24}$) or very large ($\sim 10^{33}$) numbers, PLUTO works with non-dimensional, arbitrary units. The basic units used in our simulations are length (L_0) = 1 kpc, velocity (v_0) = 100 km s^{-1} and density (ρ_0) = 1.67×10^{-23}gm cm^{-3} = 10 m$_p$ cm^{-3}. All other units are derived from these basic units as time (t_0) = L_0/v_0 = 9.8 Myr and pressure (p_0) = $\rho_0 v_0^2 = 1.67 \times 10^{-9}$ dyne cm^{-2}. Therefore, the rate of energy and mass injection to the spherical starburst region (using Eq. 9 and 10) can be written in terms of pressure and density as

$$\dot{p} = \frac{2}{3}\frac{\mathcal{L}}{(4\pi/3)\ r_{\rm inj}^3} = 9.7 \times \left(\frac{\mathcal{L}}{10^{40}\ {\rm erg\ s^{-1}}}\right)\left(\frac{100\,{\rm pc}}{r_{\rm inj}}\right)^3\ p_0/t_0 \qquad (11)$$

$$\dot{\rho} = \frac{\dot{M}_{\rm inj}}{(4\pi/3) r_{\rm inj}^3} = 0.118 \times \left(\frac{\mathcal{L}}{10^{40}\ {\rm erg\ s^{-1}}}\right)\left(\frac{100\,{\rm pc}}{r_{\rm inj}}\right)\ \rho_0/t_0 \qquad (12)$$

where, p_0, ρ_0 and t_0 are the code units of pressure, density and time respectively.

4 RESULTS

In this section we present our simulation results on the effect of outflows with different mechanical luminosities. Figure 2 shows the evolution of density and temperature for the zoomed-in (box size of 30×30 kpc^2) fiducial run ($\mathcal{L} = 10^{42}$erg s^{-1}). It shows the standard stellar wind structure, with a free wind (Chevalier & Clegg 1985) in the inner region characterised by dilute gas with high velocity, surrounded by the shocked wind and the shocked ISM. After breaking out from the disk, the free wind forms a conical shape, because of the interaction with the halo gas. The shocked wind and the shocked ISM form a multiphase structure. Because of radiative cooling, parts of this interaction zone with high density gas breaks into smaller clumps and forms clouds which are then carried away by the outflow or they fall back towards the galactic center due to gravity.

Similar wind structure is found in general for all mechanical luminosities. However, for low luminosity cases, because of the relatively low pressure in the central region, the disk material can press inwards after a certain time. Figure 3 shows one such example for $\mathcal{L} = 10^{41}$ erg s^{-1} where, at 40 Myr, the advancement of the disk material almost completely covers the injection region (at a scale of $\sim$ 1 kpc). The increase in pressure, because of the continuing injection of energy and mass, thereafter blows away the disk material and forms a filamentary multiphase outflow. We discuss the characteristics of these clouds and filaments later in §4.4. The interference of the disk material into the base of free wind can also add ripples to the conical shape of the free wind as witnessed in Figure 2.

After injection is switched off ($t > 50$ Myr), the free wind disappears and the inner region develops a complex density and velocity structure, which then gradually falls back towards the galactic center as shown in Figure 4. The forward shock, however, keeps propagating through the halo medium, finally becoming an acoustic disturbance of the medium for lower luminosities ($L \lesssim 10^{42}$ erg s^{-1}). The material that falls back to the center with non-zero velocity, collides with other gas clumps and generates secondary shocks which then push the infalling material away (lower panel of Fig. 4). After few such bouncing back and forth, the gas finally settles down at the center to form a disk-like structure (right-bottom panel of Fig. 4). In this whole process of infall and outflow, some dilute ($\rho \sim 10^{-5}$ m$_p$cm^{-3}) and hot ($T \sim 10^7$K) gas is left behind in the halo in the form of eddies. This gas neither takes part in outflow nor contributes to infall, rather becomes a part of the circumgalactic medium via dynamical mixing.

Quantitatively, the parameters of interest are, 1) the mass loading factor, which tells us the amount of mass that goes out of the virial radius, 2) the temperature distribution of the outflowing material, which holds the information regarding the various phases of the gas, and which determines the observability of these phases. 3) the velocity structure, which gives an overview of the motions of different gas phases and the coupling between them. We will discuss these properties, below, one by one.

4.1 Mass loading factor

The mass outflow rate across a spherical shell of radius r can be written as

$$\dot{M}_{\rm out}\,(r,t) = 4\pi r^2 \int_0^{\pi/2} (\rho v_r)\sin\theta\, d\theta\,, \qquad (13)$$

where θ is the zenith angle. Note that the velocity v_r in the integrand has both positive and negative values, so that, after integrating, it gives the net mass outflow rate. This outflow rate is finally integrated over time to obtain the total amount of outflowing mass ($M_{\rm out}$) at each radius for different luminosities.

This mass outflow can be compared with the total mass of new stars formed (M_*^+), and one defines a mass loading factor as

$$\eta(r,T) = \frac{M_{\rm out}}{M_*^+} = \frac{1}{M_*^+}\int_0^T \dot{M}_{\rm out}(r,t)\, dt\,. \qquad (14)$$

The choice of the integration time, T, depends upon the spatial scale of interest and is discussed later in this section.

Figure 5 shows the evolution of the mass outflow rate $\dot{M}_{\rm out}$ in units of starburst SFR at two different radii, r = 16, 160 kpc (shown with red (thick) and blue (thin) lines), as a function of time (in Myr) for three different injection luminosities, $10^{41,42,43}$ erg s^{-1} (shown with dot-dashed, double dotted and solid lines, respectively). Consider the blue and red dot-dashed lines, denoting the evolution of $\dot{M}_{\rm out}$ for $L = 10^{41}$ erg s^{-1} with time. We find that a shell of shocked ISM and shocked wind travels outward, reaching $\sim$ 160 kpc (blue) in $\sim$ 600 Myr. The negative values of $\dot{M}_{\rm out}$ corresponds to infall, which at the very outer radii arises due to acoustic

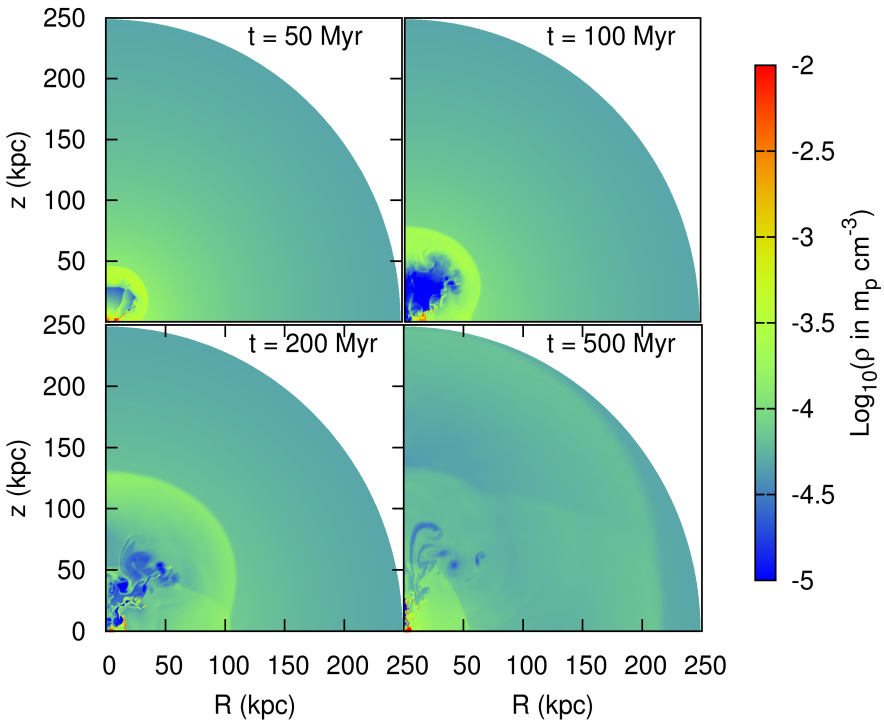

Figure 4. Density distribution at 50, 100, 200 and 500 Myr for $\mathcal{L} = 10^{43}$ erg s^{-1} for a box size of $r_{\rm max} = 250$ kpc. Note that these plots are on a scale ~ 10 times larger than the ones in Figures 2 & 3.

oscillations of the halo gas, but at inner radii corresponds to the infall of gas due to various instabilities. The interaction region between the halo and the wind suffers from thermal and Kelvin-Helmholtz instabilities, as well as the Rayleigh-Taylor instability when there is acceleration (Fraternali et al. 2006; Sharma et al. 2014). These instabilities are the key mechanisms behind the formation of clouds, some of which are the part of a galactic fountain.

The time integrated outflowing mass presents a less chaotic behaviour. In Figure 6 we show the time integrated values of the mass loading factor η (eqn 14) for our fiducial run ($\mathcal{L} = 10^{42}$ erg s^{-1}), integrated over different periods for each distance (shown in different colours/styles). The figure shows the gradual outward progression of the outflowing material in the halo. E.g., the shell reaches a distance of ~ 50 kpc in 100 Myr, and finally reaches the virial radius at a time scale of ~ 800 Myr. The figure also shows that the mass loading factor in the inner region can have small values when integrated over a long time scale, because of the infall of material in absence of injection. Therefore the behaviour of η at the inner region can be better understood if it is integrated over an appropriate, and short time scale (~ 100 Myr). On the contrary, for the mass loading factor near the virial radius, it is reasonable to average it over a long ($\sim$ Gyr) time scale. The mass outflow at smaller scale is commonly compared with the current (ongoing) star formation process. However, since the effect of central starburst reaches the virial radius only after sufficient time has elapsed (the travel time, $\sim$ Gyr), the mass outflow at large radii cannot be connected to the present day star formation. Instead, it should be compared with the past SF which caused it (i.e. the injection epoch). We define the outer mass loading factor (to be precise, the mass loading factor at virial radius) as $\eta_v = \eta(r_{\rm vir}, t_v)$, where the integration time t_v is the roughly the time taken by outflow to reach 200–230 kpc. Depending on the luminosity, t_v varies from 750 Myr to 900 Myr. In order to evaluate the inner mass loading factor we take integration time $t_v = 100$ Myr. Since the shell of outflowing material reaches a distance 20–50 kpc in 100 Myr, we denote the inner mass loading factor as η_{20}. The outflow is mainly contributed by a shell of mass moving out through the medium (Figure 6). Therefore, we take the peak value of the shell as the mass loading factor at that epoch.

The dependence of these two values of η (i.e. η_{20} and η_v) on $\mathcal{L}$ is shown in the left panel of Figure 7, where the red open squares show the values of η_{20}, appropriate for the inner region, and the blue filled squares show η_v, the values at the virial radius. The curves show that in the inner regions, the mass loading factor decreases with $\mathcal{L}$, ranging between

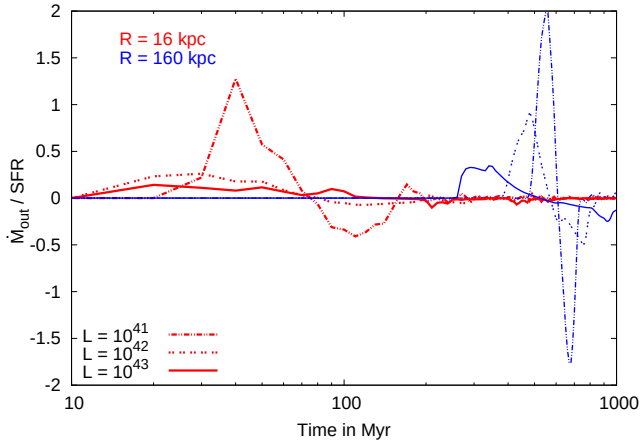

Figure 5. The evolution of the mass outflow rate in the units of starburst SFR at two different radii, 16 kpc (red, thicker lines) and 160 kpc (blue, thinner lines) as a function of time (in Myr) for different luminosities (shown in different line styles: 10^{41} erg s^{-1} (dot-dashed), 10^{42} erg s^{-1} (double dotted) and 10^{43} erg s^{-1} (solid). The results are for a simulation box size of $r_{\rm max} = 250$ kpc.

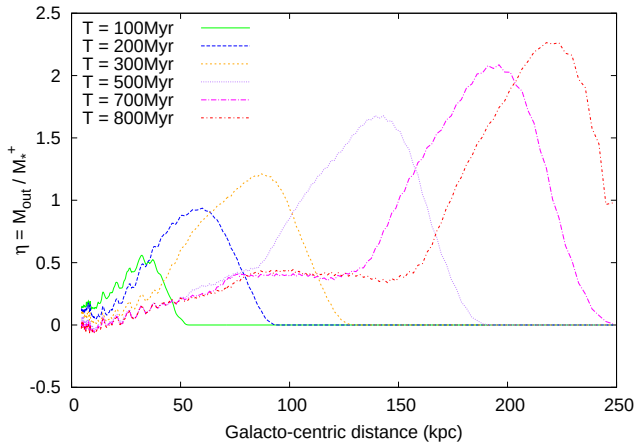

Figure 6. Mass loading factor (η) as a function of the galacto-centric radius, for $\mathcal{L} = 10^{42}$ erg s^{-1}. The values of η shown in different colours/styles correspond to different periods of integration time, from 100 Myr to 800 Myr.

~ 0.3–1, with an approximate power-law scaling $\eta \propto \mathcal{L}^{-0.25}$. The values at the outer radii also scale with $\mathcal{L}$ with a similar power-law index, and ranges between $\eta \sim 1.0$–5.0. The negative slope of η can be understood with very simple arguments. Consider a blast wave with energy E propagating in an uniform density medium. The shock radius and velocity can be given as $r_{os} \sim E^{1/5}$ and $v_{os} \sim E^{1/5}$ at any particular time. Therefore the mass outflow rate inside the shell can be written as $\dot{M}_{\rm out} \sim r^2\, v$ which in turn gives $\dot{M}_{\rm out}/E \sim E^{-2/5}$, which is equivalent to the mass loading factor we have defined here. Hence, the negative dependence of η on $\mathcal{L}$ appears naturally. Physically, explosions with smaller $\mathcal{L}$ produce an outflow that is strongly coupled to the halo gas, because (a) of low speed and (b) small conical angle in which the outflow is confined. Strong explosions, on the other hand, tend to propagate through the halo gas quickly, sweeping it with high speed, instead of much coupling.

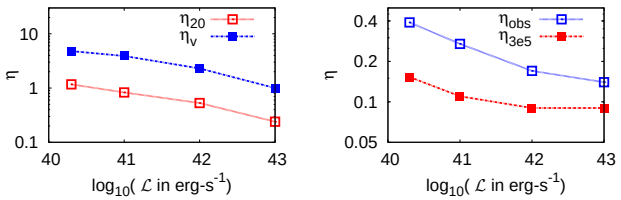

Figure 7. Left panel: The mass loading factor (η) at smaller radii (red open squares) and at virial radius (blue filled points) based on large-scale runs. Right panel: Observational mass loading factor (Eq. 18) based on small-scale runs. The blue open squares show the total $\eta_{\rm obs}$ and red filled squares show the warm mass loading factor.

We have checked that in the absence of the hot halo gas, the mass-loading factor η approaches 0.1 in the whole range of $\mathcal{L}$ considered here. It is connected with the fact that the typical mechanical luminosities in active central starbursts are always much higher than the critical luminosity necessary to break through the galactic ISM disk : $\mathcal{L}_{\rm cr} \sim 10^{38}$ erg s^{-1} for the ISM parameters used above (Nath & Shchekinov 2013). Once the wind breaks out of the disk, there is no halo resistance to stop it. Therefore, the total outflowing mass is equal to the injected mass, and the mass loading factor becomes equal to the injection value ($\eta_{\rm inj}$), 0.1 (see Fig. 11).

4.2 Effect of multiple bursts and injection time

So far we have considered the effect of a single starburst (injecting from $t = 0$ to 50 Myr). The real situation may, however, differ in particular cases as there may be multiple bursts at the centre, or the injection time period may differ. We consider two extreme cases. First, in which the active star formation periods are well separated in time from each other, i.e. they are almost independent event. In the second case, the star bursts are so close in time that they can be considered as a continuous event. We use our fiducial run to compare with the other variants (with different $\mathcal{L}$ and t_{inj}).

The first case is implemented by putting starbursts of $\mathcal{L} = 10^{41.3}$ erg s^{-1} with $t_{\rm inj} = 50$ Myr at large time separation. We put five such starbursts at the centre separated by 200 Myr in time so that the total injected energy becomes equal to the fiducial value ($\mathcal{L} = 10^{42}$ erg s^{-1}). We have calculated the average mass outflow rate as, $\langle \dot{M}_{\rm out}(r) \rangle = \frac{1}{T_{\rm avg}} \int_0^{T_{\rm avg}} \dot{M}_{\rm out}\, dt$, where $T_{\rm avg}$ is varied between 700 Myr and 1 Gyr. This choice of $T_{\rm avg}$ is motivated by the fact that the shell corresponding to the first burst takes roughly a Gyr to reach the virial radius, and subsequent shell lags behind it by roughly 200 Myr. The result of such bursts is shown in Fig. 8. The figure clearly shows that the individual outflowing shells corresponding to the independent starbursts move through the halo medium almost uninterrupted by the previous bursts and create the

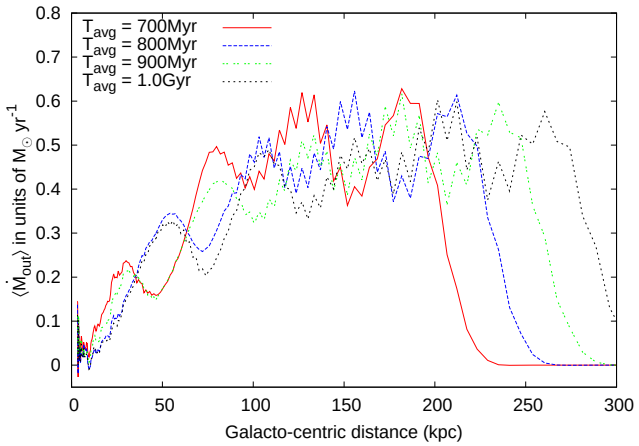

Figure 8. Effect of multiple bursts, each of $\mathcal{L} = 10^{41.3}$ erg s^{-1} and $t_{\rm inj} = 50$ Myr, on the time averaged mass outflow rate, $\langle \dot{M}_{\rm out} \rangle$, at each radius. The individual peaks corresponding to the individual starburst events show almost similar behaviour. The box size in this case is $r_{\rm max} = 350$ kpc.

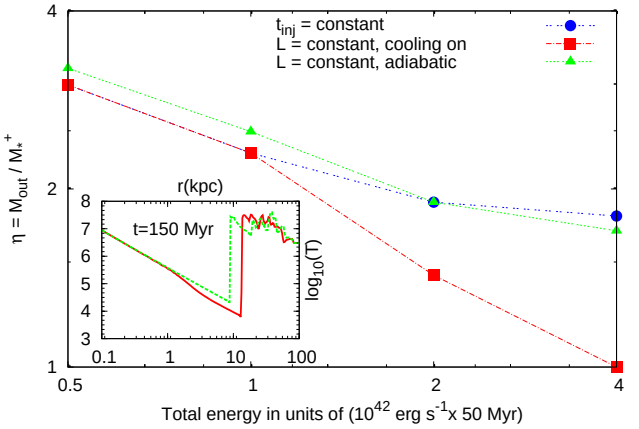
t_inj = constant
L = constant, cooling on
L = constant, adiabatic
r(kpc)
t=150 Myr
log10(T)
η = M_out / M_*^+
Total energy in units of (10^42 erg s^-1 x 50 Myr)

Figure 9. The effect of increasing energy on the mass loading factor η_v is shown by increasing the injection time and injection mechanical luminosity. The blue dots show the results when the injection time is constant ($t_{inj} = 50$ Myr) and luminosity is varied. The red squares show the result when the mechanical luminosity constant ($\mathcal{L} = 10^{42}$ erg s^{-1}) but energy is increased by increasing the injection time. The green triangles show the run for variable $t_{\rm inj}$, but, with cooling switched off. The inset shows the temperature profiles at $t = 150$ Myr for $t_{\rm inj} = 200$ Myr run. The red (solid) line corresponds to the case where radiative cooling is switched on, and the green (dotted) line represents the case where radiative cooling is absent.

same effect as it would have done for a single burst of $\mathcal{L} = 10^{41.3}$ erg s^{-1}. Hence, multiple starbursts separated by a long time interval can be treated in the same way as we treat an individual burst.

In order to understand the effect of $t_{\rm inj}$ on η_v, we use $\mathcal{L} = 10^{42}$ erg s^{-1} with different injection times ($t_{\rm inj}$) of 25, 100, and 200 Myr. The increment in the injected energy due to the increased $t_{\rm inj}$ gives rise to lower mass loading factor compared to the constant $t_{\rm inj}$ cases. The values of η_v for these cases depend on the total energy as $\eta_v \propto \mathcal{E}^{-0.5}$ (see Fig. 9), where $\mathcal{E} = \mathcal{L} \times t_{\rm inj}$. Figure 9 shows that η_v decreases when the injection time lasts for more than $\sim$ 50 Myr compared to runs which have same energy but where the injection lasts only for 50 Myr.

A comparison with the adiabatic counterparts of these runs (shown by the green triangles in Fig. 9) shows that this decrease in the mass loading factor can be attributed to the radiative cooling of the free wind which lasts long enough ($>$ 50 Myr) to radiate away a significant fraction of the total energy. The inset of Fig. 9 shows the temperature profiles of a (10^{42}, 200 Myr) run at $t = 150$ Myr. This plot shows the decrease of temperature (or the internal energy) due to radiative losses in the free wind. Thus it is evident that if the free wind phase lasts for a long time (due to prolonged injection time), then it radiates away a good fraction of the energy.

The above results allow us to write the variation of η_{20} and η_v as a function of the total energy or total mass of stars formed within the injection time (obtained from the fits of Fig. 7) as

$$\eta_{20} \approx 0.4 \times \left(\frac{\mathcal{E}}{\mathcal{E}_F}\right)^{-0.25} = 0.4 \times \left(\frac{M_*^+}{M_*^F}\right)^{-0.25}, \qquad (15)$$

and

$$\eta_v \approx 2.5 \times \left(\frac{\mathcal{E}}{\mathcal{E}_F}\right)^{-0.25} = 2.5 \times \left(\frac{M_*^+}{M_*^F}\right)^{-0.25}. \qquad (16)$$

where, $\mathcal{E}_F = 10^{42}$ erg s^{-1} $\times$ 50 Myr is the energy for the fiducial run and M_*^F(= 14.0 M$_\odot$ yr^{-1} $\times$ 50 Myr) is the corresponding mass of new stars formed. However, for long $t_{\rm inj}$ ($\gtrsim$ 50 Myr) in case of $\mathcal{L} > 10^{42}$ erg s^{-1}, the cooling affects the dynamics and the mass loading factor can be written as

$$\eta_v \approx 2.5 \times \left(\frac{\mathcal{E}}{\mathcal{E}_F}\right)^{-0.5} = 2.5 \times \left(\frac{M_*^+}{M_*^F}\right)^{-0.5}. \qquad (17)$$

4.3 Comparison with observed mass loading factor

We compare the values of η obtained from our simulations with those estimated from observations, where only partial information about the velocity and density structure is available. The mass loading factor in observations is defined as $\eta = \frac{M \times v_r}{r \times \rm SFR}$, where, M is the total mass of outflowing gas (observed as molecular or ionised gas), r is the typical scale of the outflowing region and v_r is an estimate of the outflowing gas velocity (Arribas et al. 2014; Bolatto et al. 2013) or the sound speed (Stickland & Heckman 2007). In order to compare with the observed values of mass loading factor, we define $\eta_{\rm obs}$, the mass loading factor within a outflowing region of radius r_d at any time t as

$$\eta_{\rm obs}(r_d, t) = \frac{M\, v_r}{\rm SFR}\, \frac{1}{r_d} = \frac{1}{\rm SFR}\, \frac{2\pi}{r_d} \int_0^{r_d} r^2\, dr \int_0^{\pi} (\rho v_r)\, \sin\theta\, d\theta\,, \qquad (18)$$

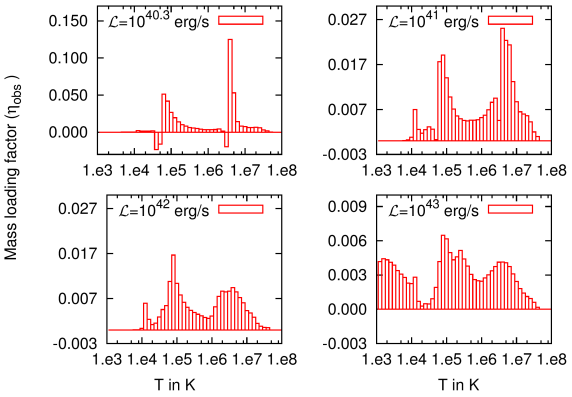

Figure 10. Temperature distribution of the outflowing gas for different luminosities at a galacto-centric radius 10 kpc, averaged over 50 Myr.

where, r_d is taken to be 10 kpc, the radius within which most of the observations are limited. It is to be noted that the velocity inside the integral is the actual velocity of any individual fluid packet rather than some characteristic speed of the whole fluid as usually considered by the observations. Since, during a starburst the mass outflow rate is not constant because of the halo-wind interactions and formation of clouds and eddies, to get a reliable value, and to connect with the current SFR, we average it over the injection period (50 Myr). The values of time averaged $\eta_{\rm obs}$ is shown in the right panel of Figure 7 by the blue open squares. These values show the same behaviour as seen previously in η_{20} only with a shallower dependence on $\mathcal{L}$ ($\eta_{\rm obs} \propto \mathcal{L}^{-0.15}$).

However, the estimation of the mass loading factor from observations is either for the cold molecular gas (Bolatto et al. 2013) or the ionised (Arribas et al. 2014) or the hot gas (Stickland & Heckman 2007), and not for all the phases taken together. Therefore, to determine the mass loading factors for different phases and find the correlation between them, it is important to study the temperature distribution of $\eta_{\rm obs}$. Figure 10 shows that the outflowing mass is divided mainly into two temperature domains, one at $\sim 10^5$ K, and, another at $\sim 5\times10^6$ K. The 10^5 K gas comes from the evaporation of the disk gas and adiabatically expanded wind material, and, the hot gas (T $\sim 5\times10^6$ K) comes from the shocked ISM and wind material. We also notice a small peak near $T = 10^4$K, which arises because of the clouds formed from the interaction between wind and halo material and from the condensation of the evaporated disk material. The extended outflowing gas at $T < 10^4$ K in case of $\mathcal{L} = 10^{43}$ erg s^{-1} arises due to the adiabatic cooling of the free wind (see right-bottom plot of Figure 10).

The temperature plots imply that observations aimed to detect either the cold or ionised or hot gas are likely to miss a significant fraction of the outflowing material even at small radii. Therefore, to determine the contribution of the warm gas which is the commonly used observational tracer of outflow, we define a new mass loading factor $\eta_{\rm 3e5}$ which counts only $T < 3\times10^5$ K gas. This is represented by red filled squares in the right panel of Figure 7, which also shows that $\eta_{\rm 3e5}$ is less than the total mass loading factor $\eta_{\rm obs}$ by a factor of 2–3. Moreover, the mass loading factor is almost equal to the injection value, 0.1 (see §3.1), which is of a similar magnitude as estimated by Arribas et al. (2014) in case of MW type galaxies (dynamical mass $\sim 10^{11} M_\odot$).

To understand the relations between different mass loading factors we have fitted them with simple power-law relations:

$$\eta_{\rm obs} \simeq 0.4\times\mathcal{L}_{40}^{-0.15} \simeq 0.3\times\left(\frac{\rm SFR}{\rm M_\odot\ yr^{-1}}\right)^{-0.15}, \quad (19)$$

$$\eta_{\rm 3e5} \simeq 0.15\times\mathcal{L}_{40}^{-0.1} \simeq 0.12\times\left(\frac{\rm SFR}{\rm M_\odot\ yr^{-1}}\right)^{-0.1}. \quad (20)$$

Comparing these equations with Eq. 16 and using Eq. 9, we can write

$$\eta_v \approx 5\times\left(\frac{\rm SFR}{\rm M_\odot yr^{-1}}\right)^{-0.25}\times\left(\frac{t_{\rm inj}}{\rm 50Myr}\right)^{-0.25} \approx 40\times\left(\frac{\rm SFR}{\rm M_\odot yr^{-1}}\right)^{-0.15}\times\left(\frac{t_{\rm inj}}{\rm 50Myr}\right)^{-0.25}\times\eta_{\rm 3e5}. \quad (21)$$

This gives a relation between the warm mass loading factor, $\eta_{\rm 3e5}$ (relevant for observations), and the outer mass loading factor (η_v) (relevant for cosmological scales) for a given starburst period and SFR. Eq. 21 shows that the mass loading factor at the virial radius is larger by a factor ~ 40 than the mass loading factor that is observable near the central region. This relation is almost independent of SFR but depends upon the starburst activity time.

The ratio $\eta_v/\eta_{\rm 3e5}$ also depends on the baryon fraction of the galaxy, in particular, the fraction of the total mass that is in the form of halo gas. Since the main contribution to the outflowing mass at the outer radii comes from the swept up halo material, the outer mass loading factor strongly depends on the mass budget of the background halo gas. Figure 11 shows the variation of η_v as a function of the baryon fraction (f_b). The figure shows that, for $f_b \gtrsim 0.1$ i.e. when more than half of the baryon is in the hot halo phase, η_v varies weakly with f_b. However, for $f_b \lesssim 0.1$, mass loading factor decreases steeply and finally for $f_b = 0.05$ (the stellar mass fraction), it becomes equal to the injection value, 0.1. Therefore, $\eta_v/\eta_{\rm 3e5}$ can vary between $\sim$ 1–40 depending on the baryon fraction.

In this paper, we have only varied the mechanical luminosity and injection time; the other parameters like total galactic mass have been kept fixed. The observational scaling of η(SFR), on the other hand, may be contaminated by these additional variables. Indeed, a larger mechanical luminosity suggests, in general, a higher star formation rate, which in turn may indicate a larger galactic mass, and a more massive and extended hot halo.

We have also carried out simulations at various resolutions, and we find excellent convergence for the various mass loading factors (η_{20} & η_v) in case of the large-scale runs. The small-scale runs, which study the multiphase gas, are somewhat resolution-dependent as they do not resolve the transi-

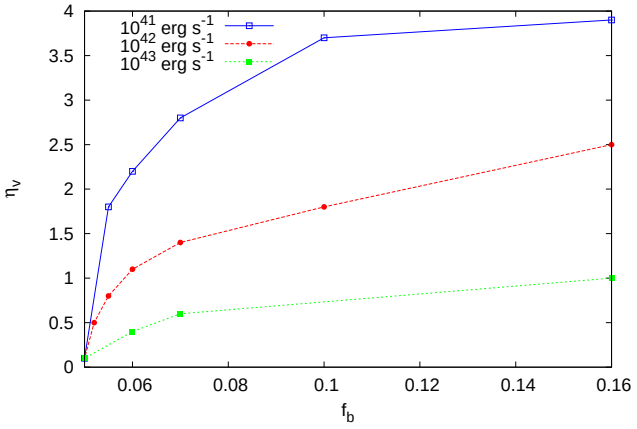

Figure 11. Variation of outer mass loading factor (η_v) with baryon fraction of the galaxy in the case of different luminosities of $\mathcal{L} = 10^{41,42,43}$ erg s^{-1} (or runs L1, L2 and L3 in Table 2).

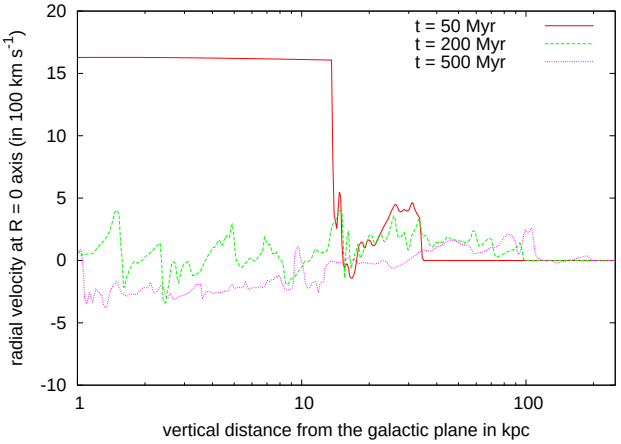

Figure 12. Velocity profiles along $R = 0$ axis at 50, 200, 500 Myr for the case of $\mathcal{L} = 10^{42}$ erg s^{-1}.

tion regions between the cold and hot phases in the absence of thermal conduction (see Koyama & Inutsuka 2004). However, the relation between the mass loading factors in Eq. 21 holds within a factor of two for all resolutions.

4.4 Velocity structure

Figure 12 shows the velocity profiles at three different epochs (50, 200, 500 Myr) along the vertical direction ($R = 0$) for the fiducial run ($\mathcal{L} = 10^{42}$ erg s^{-1}). The red solid curve for the profile at 50 Myr (when the injection is still on) shows the structure of a standard luminosity-driven wind, with an inner region of free wind travelling at high speed, which is surrounded by the shocked wind, and then by the shocked ISM, which drives an outer shock through the ambient medium. After this period (50 Myr), when the injection stops, the interaction zone produces clumps which sometimes fall back and create regions with negative velocity. However, the outer shock continues to propagate through the ambient gas and reaches a distance of 200 kpc in 500 Myr in this case. The speed of the hot gas in the interior region depends crucially on the assumption of the mass loading factor at injection, and in the case of $\dot{M} = 0.1$ SFR, it reaches 1600 km s^{-1}. This is consistent with the analytical velocity of luminosity driven winds ($\sqrt{2\mathcal{L}/\dot{M}}$; e.g., Sharma & Nath 2013, Chevalier & Clegg 1985). We also note that, although the initial speed of the outflowing gas is $\sim$ 1000 km s^{-1} or above, it is not sustained for long and at later times when injection is turned off, the velocity becomes so small that it can be considered as a sound wave moving through the hot medium. This can be seen in Figure 13 which plots the Mach number of the gas as a function of distance at 500 Myr for different luminosities. The Mach number of the outflowing gas at large distances decreases to $\lesssim 1$, for the mechanical luminosities considered here. Therefore the outflows eject the gas out of the virial radius with speeds comparable to the sound speed

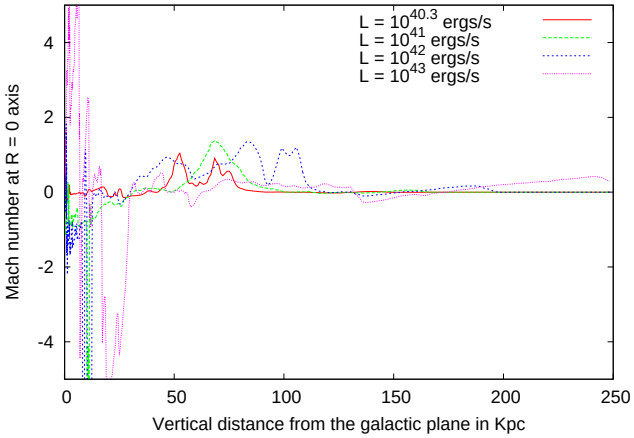
L = $10^{40.3}$ ergs/s
L = 10^{41} ergs/s
L = 10^{42} ergs/s
L = 10^{43} ergs/s
Mach number at R = 0 axis
Vertical distance from the galactic plane in Kpc

Figure 13. The Mach number profiles along the $R = 0$ axis at 500 Myr for different luminosities.

of the halo gas. This has important implications for the enrichment models of the IGM. Next, we focus on the wind structure at observable scales ($\sim$ 10 kpc) based on our small-scale/short-duration simulations.

While ploughing through the ISM, the wind fluid entrains the warm disk gas with it. For low luminosities ($\lesssim 10^{41}$ erg s^{-1}) this entrained gas mixes with the wind and forms filaments and cloud-like structures embedded within the 10 kpc free wind. For higher SFR, the disk gas is mainly located near the contact discontinuity of wind cone. While being carried away by the high velocity wind, a fraction of the cold clumps gets evaporated and the rest propagates outwards due to the ram pressure of the free wind. Therefore, the dynamics of the clouds and filaments is momentum conserving, for which the velocity increases with the distance (Murray et al. 2005). As the density of the hot gas decreases with distance, the ram pressure decreases, leading to an asymptotic speed of the clouds. However, this result pertains to a steady state sit-

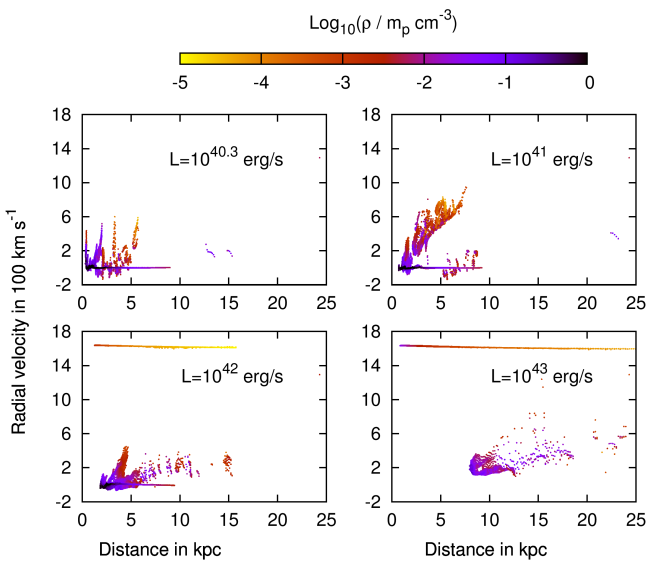

Figure 14. Scatter plot of the velocity of the warm gas ($T < 3 \times 10^5$ K) and radial distance at 50 Myr. Top panel is for $\mathcal{L} = 10^{40.3}$, 10^{41} erg s^{-1} and bottom panel is for $\mathcal{L} = 10^{42}$ and 10^{43} erg s^{-1} respectively.

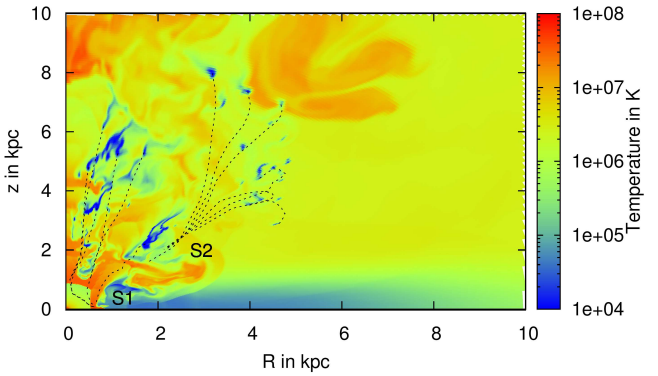

Figure 15. Temperature map for $\mathcal{L} = 10^{41}$ erg s^{-1} at 50 Myr for, on which we superpose the tracks for cold clouds. The main sequence (S1) clouds (entrained by high velocity free wind) are tracked back for 17 Myr, and the secondary sequence (S2) clouds (entrained by the low velocity shocked wind) are tracked back for 40 Myr.

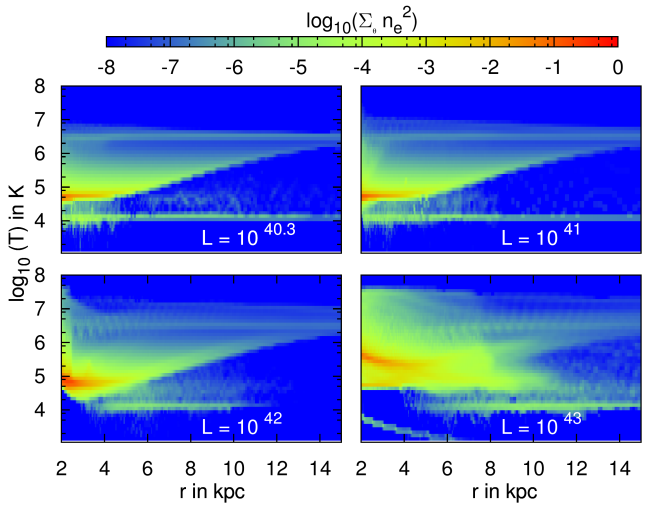

Figure 16. Scatter plot of temperature and radial distance of gas particles, colour coded by the time average of density squared (averaged over 50 Myr), shown for four different mechanical luminosities.

uation, which is not the case here. The result obtained here is suitable for comparing the cloud kinematics at a particular time as obtained in observations.

Figure 14 shows the position and velocity of warm/cold gas ($T < 3 \times 10^5$ K) for four different luminosities at 50 Myr. The figure shows that the velocity of the cold and warm gas ranges from ~ -150 km s^{-1} to ~ 800 km s^{-1}. The points with constant velocity at $\simeq 1600$ km s^{-1} represent the adiabatically cooled free wind in case of $\mathcal{L} = 10^{42}$ and 10^{43} erg s^{-1}, while the points with nearly zero velocity represent the stationary disk gas.

For $\mathcal{L} = 10^{41,42}$ erg s^{-1}, we also notice two sequences of velocity points, one which is a dominant sequence (referred to as the main sequence here), which extends from zero velocity to a velocity of ~ 800 km s^{-1}, and, a secondary sequence which is almost parallel to the main sequence but extends from -150 km s^{-1} to $+200$ km s^{-1}. Both sequences are almost linearly dependent on the radius. This can be understood as the effect of ram pressure of the outgoing free/shocked wind, as mentioned previously. The radial dependence of the velocity of the warm gas in our simulation can be compared with the results obtained by Shopbell & Bland-Hawthorn (1998) in case of H_α filaments in M82, who also observed a roughly linear relation between velocity and height above the disk (their Figure 10).

The origin of these two sequences are quite similar. The main sequence is entrained by the high velocity free wind, thereby giving it a relatively higher velocity. On the other hand, the secondary sequence arises because of the entrainment of the clouds by the lower velocity shocked wind. As shown in the evolution of wind for $\mathcal{L} = 10^{41}$ erg s^{-1} in Figure 3, the main sequence corresponds to the clouds formed after the disk material advances inwards and is blown away into a filamentary structure (see snapshots at 40 and 50 Myr in Figure 3). The second sequence of clouds corresponds to the ones formed in the interaction zone between the hot halo gas and shocked ISM due to various instabilities like thermal, Rayleigh-Taylor instabilities. (see Fig. 2).

Figure 14 also shows the cloud gas density in colours. The clouds at large distances are in general more tenuous than those at inner region, which can be understood from adiabatic expansion of clouds moving in an ambient medium (free wind) whose pressure decreases with distance.

The extension of the secondary sequence from ~ -150

km s^{-1} to +200 km s^{-1} means that few clouds are also falling back to the centre. The fraction of mass that falls back to the center, however, is small to trigger any noticeable star formation, as will be discussed in the next section. Figure 15 shows the time tracks of these two sequences of clouds seen at 50 Myr for $\mathcal{L} = 10^{41}$ erg s^{-1}. The main sequence (labelled S1) are tracked back for 17 Myr, and represents relatively younger disk material, whereas the secondary sequence clouds (S2) are tracked for 40 Myr, which are basically older population clouds. These two families of tracks clearly shows the source of the clouds and supports our previous discussion about their origin in the free and shocked wind. Other than these two sequences, we also notice some island points (in Figure 14) at a galacto-centric radius of $\sim$ 15–25 kpc having velocity close to $\sim$ 400 km s^{-1}, which may represent rare high velocity-high latitude clouds as observed by Sembach et al. (2002).

Figure 16 shows the temperature and position of gas parcels, colour coded by the time average of the square of particle density (averaged over 50 Myr), for four different mechanical luminosities. Only the parcels of gas within 15 kpc are represented here. The two horizontal streaks at $10^{6.5}$ K and 10^4 K corresponds to the hot halo and warm clouds, respectively, whereas the rising envelope of increasing temperature with radial distance corresponds to the mixture of the disk and halo gas in the plane of the disk. The $1/r^2$ fall of temperature in case of $\mathcal{L} = 10^{43}$erg s^{-1} is easily understood as the adiabatically expanding gas. The regions marked in red and orange (back and deep gray in gray-scale) correspond to gas with high emissivity, and therefore are important from the consideration of observability. The figure suggests that for very low luminosity outflows, most of the emission would arise from gas at $\sim 10^5$ K gas within $\sim$ 5 kpc. X-ray emitting gas becomes important for $\mathcal{L} \geqslant 10^{42}$ erg s^{-1}, corresponding to SFR of $\sim$ 10 M$_\odot$ yr^{-1}. These results are consistent with observations of X-rays from outflows (Stickland & Heckman 2007), including the X-ray emission from the outflow in Milky Way (Snowden et al. 1995; Breitschwerdt & Schmutzler 1994).

4.5 Mass inventory

In addition to the mass loading factor, the velocity and the temperature distribution, we have also estimated the total outflowing mass. This is an important parameter in the context of the evolution of the galactic disk and halo, as well as the enrichment of the IGM. The total mass injected into the halo is assumed to be proportional to the SFR or $\mathcal{L}$ (Eq. 10), and it is a small fraction of the gas mass in the halo, even for the largest SFR considered here. However, the total mass of the outflowing gas ranges between 0.2–10% of the total gas content (10^{11} M$_\odot$), increasing roughly linearly with SFR, between 1.5–150 M$_\odot$ yr^{-1}. Therefore outflows corresponding to large SFR can change the halo gas density by $\leqslant$ 10%. We have also found that the average disk mass does not change appreciably by either ejection or fall back of gas ($\leqslant$ 1% for the most vigorous outflows) and in all cases, the change in the disk mass is much smaller than the injected mass. Previous works have discussed the role of the halo gas in massive galaxies either suppressing or triggering star formation in the disk by absorbing the outflowing gas or pushing it back on to the disk, respectively.The massive halo is expected to play an important role in quenching star formation in massive galaxies by cutting off the supply of fresh cooling gas. The halo also suppresses appreciable fall back of outflowing gas and quenches star formation, although the detailed mechanism of such quenching remains uncertain (Gabor & Davé 2014; Oppenheimer et al. 2010). The above mass estimation implies that the injected material mostly gets deposited in the halo. Hence these outflows do not trigger further star formation by recycling mass to the disk (e.g., as in a galactic fountain). In other words, outflows in the presence of an extended hot halo gas can quench star formation in the galaxy.

5 DISCUSSION

We discuss a few implications of our results presented in the preceding sections.

5.1 Definition of mass loading factor

We have defined the mass loading factor here as the ratio between the total outflowing mass and the total mass of stars formed. This is in contrast with the usual definition, as the ratio between the mass outflow rate to the *current* SFR. Our definition is motivated by the fact that by the time the outflowing mass reaches the outer halo, its dependence on the *current* SFR loses its significance, since the duration of the SFR ($t_{\rm inj}$) is usually much smaller than $\sim$ 1 Gyr, the time taken by the outflow to reach the virial radius. However, these two definitions are related to each other, and here we briefly discuss their inter-relation.

These two definitions coincide if in the case of (a) outflows at small length scales and (b) when the starburst activity last for a long time. In the first case, the observed *current* SFR is related to the cause of the outflow. In the case, if the starburst activity lasts long time ($\gtrsim$ 300 Myr) or there are repeated bursts at the centre, the outflow properties (viz. velocity, metallicity etc) at $\sim$ 100–200 kpc also can be connected to the ongoing star formation process, as observed by Tumlinson et al. (2011). Suppose one had defined the outer mass loading factor as the ratio between averaged mass outflow rate and the SFR as

$$\langle \eta_v \rangle = \frac{\langle \dot{M}_{\rm out} \rangle}{\rm SFR} = \frac{1}{\rm SFR \times t} \int_0^t \dot{M}_{\rm out}(r_v, t')\, dt' \,, \qquad (22)$$

where, t is the averaging time, which can be taken roughly equal to the time taken by the shell to reach that particular radius. This definition of $\langle \eta_v \rangle$ can be connected to our earlier definition in Eq. 14 as

$$\eta_v = \frac{M_{\rm out}}{M_*^+} = \frac{\langle \dot{M}_{\rm out} \rangle}{\rm SFR} \times \frac{t}{t_{\rm inj}} = \langle \eta_v \rangle \times \frac{t}{t_{\rm inj}} \,. \qquad (23)$$

Note that, this relation holds only when $t > t_{\rm inj}$. For $t < t_{\rm inj}$, the total mass of new stars formed is $M_*^+ = {\rm SFR} \times t$, therefore,

$\eta_v = \langle\eta_v\rangle$. The ratio $t/t_{\rm inj}$ can be estimated from our simulations as follows. The shell arrival time in our simulation can be written as $r_{sh} \approx 1.3\,{\rm kpc}\,\mathcal{L}_{42}^{1/5}\,t_{\rm Myr}^{3/4}$ which in turn gives $t/t_{\rm inj} \approx 17\,r_{200{\rm kpc}}^{4/3}\mathcal{L}_{42}^{-4/15}t_{\rm inj,50Myr}^{-1}$. Therefore, Eq. 23 gives us

$$\eta_v \approx 17\,\langle\eta_v\rangle\; r_{200{\rm kpc}}^{4/3}\mathcal{L}_{42}^{-4/15}t_{\rm inj,50Myr}^{-1}\,. \qquad (24)$$

From this equation we can clearly see that when the star formation lasts long i.e $t \approx t_{\rm inj}$, $\eta_v \approx \langle\eta_v\rangle$. In other words, the two definitions (one w.r.t. the average outflow rate, and another, presented here, w.r.t. the total outflowing mass) are equivalent in the case of long duration starbursts.

5.2 Dust in clouds

Clouds formed in the galactic outflows are not only important for containing ions that make them observable, but they can also contain dust particles. Our result shows that roughly half the outflowing mass (inside 10 kpc) resides in gas of temperature $\sim 10^6$ K and the other half in warm clouds of temperature $\sim 10^5$ K, has important implications for the types of dust particles that are likely to be embedded in outflows. The thermal sputtering rate of dust grains at 10^5 K is small, and the time scale required to destroy even the smallest dust grains ($\sim 0.003\,\mu$m) in warm clouds is ~ 15 Gyr considering a density of $\sim 10^{-3}$ m$_p$ cm^{-3} in these clouds, as inferred from the density distributions in Figures 2 and 3. These clouds can therefore preserve even the smallest grains, as long as the clouds can survive. The hotter regions in which half the mass of the outflowing gas resides, has a larger sputtering rate. At $\sim 10^6$ K, the smallest grains that can survive after 50 Myr is roughly 0.003 μm for graphites and 0.03 μm for silicates. These clouds therefore contain 'grey' dust. In other words, half the dust mass carried by outflows are likely to be rendered 'grey' during the transport from the disk to the outer halo.

5.3 Absorption study of clouds

Our Galaxy has a SFR of ≈ 3 M$_\odot$ yr^{-1}, which corresponds to a mechanical luminosity of $\sim 10^{41.3}$ erg s^{-1}. Therefore the results of simulations with $\mathcal{L} = 10^{41}$ erg s^{-1} are appropriate for comparison with our Galaxy. The numerous clouds that are formed during different stages would correspond to clouds observed in various wavelengths in the halo of Milky Way. Cold clouds with $T \leqslant 10^4$ K would correspond to HI clouds or MgII absorption clouds. The cold clouds seen in the temperature distributions in Figure 15 portray a visual impression of a likely scenario of clouds responsible for MgII absorption, although we emphasise that we do not aim to reproduce the Milky Way observations in our paper. Shooting lines of sight from the centre in the range of $\theta = 0$–70° (avoiding lines of sight within 20° of the disk), we estimate a covering fraction of $\sim 60\%$ for MgII clouds. This is consistent with the estimate of Lehner et al. (2012) for fraction of high velocity clouds with MgII, although the correspondence should be interpreted with caution.

5.4 Redshift dependence

The specific star formation rate (sSFR, defined as the SFR per unit stellar mass) of Milky Way type galaxies increases at high redshift. Weinmann et al. (2012) found the sSFR of galaxies with stellar mass $\sim 10^{10}$ M$_\odot$ to increase by a factor of ~ 20 at $z \sim 2$. The corresponding star formation time scale (1/sSFR) decreases from the current value of ~ 10 Gyr to ~ 0.5 Gyr. Therefore, the appropriate mechanical luminosity for counterparts of Milky Way at high redshift would be $\mathcal{L} \sim 10^{42.6}$ erg s^{-1}. As Fig. 7 shows, for mechanical luminosities of this order, the mass loading factor at the virial radius is close to unity.

5.5 IGM enrichment

The result that outflows leave the virial radius with a speed comparable to the sound speed of the halo gas may affect the enrichment history of the IGM. The sound speed of the halo gas at virial temperature is roughly half the escape speed at the virial radius, over a large range of masses and redshift. It is generally believed that the speed of the outflows is much larger than the escape speed. If the outflow speed is decreased as found here, then the radius of influence of the outflows in the IGM will be smaller than previously thought. However, we should note that this result holds only for large galaxies with hot halo gas, whereas most of the contribution to the enrichment of the IGM comes from low mass galaxies (e.g., Nath & Trentham 1997; Madau et al. 2001; Ferrara et al. 2000b; Oppenheimer et al. 2006), which may not harbour a hot gas in the halo.

6 SUMMARY

In this paper, we have presented an extensive numerical study of SN driven galactic outflows for a MW type galaxy. Our modelled galaxy contains a gaseous disk of $T = 10^4$ K, and an extended hot ($T = 3 \times 10^6$ K) halo gas around it. The SN feedback was implemented in the form of mechanical energy within a compact region (< 60 pc) at the center of the galaxy. We have studied the effect of such energy inputs in small scales (~ 30 kpc) and in large scales (~ 200 kpc). The small scale studies reveal the presence of multiphase structure of the outflowing material and a temperature dependent outflow rate and thus help us to connect the mass loading factor at virial radius to the observable mass loading factor.

We summarise our work as follows.

(i) *Mass loading factor*: The presence of hot halo gas in galaxies increases the mass loading factor compared to the no-halo case. In the inner region (within ~ 10 kpc), the mass loading factor can increase up to a factor of ≈ 5 compared to $\eta_{\rm inj}$ when the mass fraction of the hot halo gas is ~ 0.1. In comparison, the mass loading factor near the virial radius (η_v), can increase up to 10–40 when compared with $\eta_{\rm inj}$. For low value of baryon fraction (f_b), the mass loading factor can be as low as 0.1 (i.e. equal to the $\eta_{\rm inj}$). The effect of the halo

gas in determining outflow rate is more pronounced in case of low star formation rates compared to the higher ones.

Though we have mainly considered a single starburst of duration 50 Myr, we have also shown that multiple bursts at the center that are well separated in time, have similar effects on gas at large radii. A comparative study with different star formation periods suggests that η_v depends only on the total mass of new stars formed. However, for higher mechanical luminosity ($\mathcal{L} \gtrsim 10^{42}$ erg s^{-1}) cases, a star formation period longer than $\sim$ 50 Myr leads to significant radiative cooling and η_v in this case also depend on the injection time scale.

We also found that the hot halo gas helps to quench star formation in the disk by inhibiting any appreciable recycling of mass into the disk.

(ii) *Temperature distribution and observability*: The temperature distribution of the outflowing gas is approximately bimodal, peaking at 10^5 and $10^{6.5}$ K. This bimodality implies that half of the outflowing gas is in form of warm clouds/gas and other half is in the form of hot X-ray emitting gas. This result allows us to connect the mass outflow rate for cold/warm gas to the outflow rate at the virial radius. We find that for a SFR of $1\,M_\odot$ yr^{-1}, the total (all of it in the hot phase) mass loading factor at the virial radius is roughly 25 times the mass loading factor for cold/warm gas near the center for a baryon fraction of 0.1 and injection time $\sim$ 50 Myr.

(iii) *Velocity*: The velocity of the free wind is found to be close to $\sim$ 1600 km s^{-1} when the energy injection is still active. Velocity of the outflow decreases once the injection is switched off and for SFR $\lesssim$ 10 $M_\odot$ yr^{-1} after $\sim$ 400 Myr, it becomes comparable to the sound speed of the medium. Therefore, the velocity with which the outflow exits the galaxy is close to the sound speed of the hot medium ($c_s \sim 200$ km s^{-1}) and the density of the outflow is also close to the halo medium ($\sim 10^{-4}$ m$_p$ cm^{-3}). We also notice that, even for a SFR $\sim 150\,M_\odot$ yr^{-1}, the whole galaxy is not 'blown away'. Due to the presence of the hot halo, a strong starburst acts like only a perturbation at the center, after which, the galaxy relaxes and forms a disk -like structure again.

(iv) *Cloud velocity*: The velocity of the warm clouds in our small-scale simulations found to form two sequences in position-velocity diagram. One, extends almost linearly from 0 to $\sim$ 800 km s^{-1}, another, extends from ~ -200 to $\sim +200$ km s^{-1}. These two sequences are signature of entrainment of warm clouds by the high velocity free wind and the low velocity shocked wind respectively.

To conclude, our work focuses on the relation between the mass loading factor at various radii and connects them to the SFR without coupling it to the total mass or gas surface density of the galactic disk. Therefore, relations obtained in this paper can be used to extrapolate the observed outflow rate near the center to the outflow rate at the virial radius, for Milky Way type galaxies. A more general study of the dependence of mass loading factor on the galactic mass will be addressed in a future study.

ACKNOWLEDGEMENT

We thank Romeel Davé for his useful discussions. We also thank anonymous referee for his comments. KCS is partly supported by CSIR (grant no 09/1079(0002)/2012-EMR-I). PS is partly supported by DST-India grant no. Sr/S2/HEP-048/2012. YS is supported by RFBR (grant no. 12-02-00917).

REFERENCES

Arribas, S., Colina, L., Bellocchi, E., Maiolino, R., Villar-Martín, M., 2014, arXiv:1404.1082v1
Babul, A., Rees, M. J., 1992, MNRAS, 255, 346
Bogdán, Á., Forman, W. R., Vogelsberger, M., Bourdin, H., Sijacki, D., Mazzotta, P., Kraft, R., Jones, C., Gilfanov, M., Churazov, E., David, L., 2013, ApJ, 772, 97
Bogdán, Á., Forman, W. R., Kraft, R. P., Jones, C., 2013, ApJ, 772, 98
Bolatto, A. D, Warren, S. S., Leroy, A. K., Walter, F., Veilleux, S., Ostriker, E., Ott, J., Zwaan, M. et al.2013, Nature, 499, 450
Bordoloi, B., Tumlinson, J., Werk, J., et al.2014, arxiv: 1406.0509
Bouché, N., Hohensee, W., Vargas, R., Kacprzak, G. G., Martin, C. L., Cooke, J., Churchill, C. W. 2012, MNRAS, 426, 801
Breitschwerdt, D, Schmutzler, T. 1994, Nature, 371, 774
Chattopadhyay I., Sharma M., Nath B., Ryu D., 2012, MNRAS, 423, 2153
Chevalier R. A., Clegg A. W., 1985, Nature, 317, 44
Cooper J. L., Bicknell G. V., Sutherland R. S., 2008, ApJ, 674, 157
Dalla Vecchia C., Schaye J., 2008, MNRAS, 387, 1431
Dekel, A., Silk, J. 1986, ApJ, 303, 39
Fang, T., Bullock, J., Boylan-Kolchin, M., 2013, ApJ, 762, 20
Ferrara, A., Pettini, M., Shchekinov, Yu. A. 2000, MNRAS, 319, 539
Ferrara A., Tolstoy E., 2000, MNRAS, 313, 291
Fraternali F., Binney J. J., 2006, MNRAS, 449, 449
Gabor, J. M., Davé, R., 2014, arxiv:1405.1043v1
Gatto, A., Fraternali, F., Read, J. I., Marinacci, F., H. Lux, Walch, S., 2013, arxiv:1305.4176v2
Heald G. H., Rnad R. J., Benjamin R. A. and Bershady M. A., 2006, ApJ, 647, 1018
Heckman, T. M., Lehnert, M. D., Strickland, D. K., Armus, L. 2000, ApJS, 129, 493
Hopkins P. F., Quataert E., Murray N., 2012, MNRAS, 421, 3522
Hopkins P. F., Keres D., Onorbe J., Faucher-Giguere C-A., Quataert E., Murray N., Bullock J. S., in press , arXiv: 1311.2073v1
Kalbera P. M. W., Kerp J., 2009, ARAA, 47, 27
Koyama H., Inutsuka S., 2004, ApJ, 602, 25
Lagos, C. del P. , Lacey, C. G., Baugh, C. M. 2013, 436, 1787
Larson, R. 1974, MNRAS, 169, 229
Lehner, N., Howk, J. C., Thom, C., Fox, A. J., Tumlinson, J., Tripp, T. M., Meiring, J. D. 2012, MNRAS, 424, 2896
Leitherer, C., Schaerer, D., Goldader, J. D., Deldado, R. M. G., Robert, C., Kune, D. F., De Mello, D. F., Devost, D. and Heckman, T. M., 1999, ApJSS, 123, 3
Liou M. S., 1996, J. Comput. Phys., 129, 364
Mac Low M-M., Ferrara A., 1999, ApJ, 513, 142
Maccio A. V., Dutton A. A., Bosch F. C. van den, Moore B., Potter D., Stadel J., 2007, MNRAS, 378, 55
Madau, P., Ferrara, A., Rees, J., M., 2001, ApJ, 555, 92
Martin, C. 1999, ApJ, 513, 156
Martin, C. L., Shapley, A. E., Coil, A. L., Kornei, K. A., Bundy,

K., Weiner, B. J., Noeske, K. G., Schiminovich, D. 2012, ApJ, 760, 127
Mathes, N. L., Churchill, C. W., Kacprzac, G. G., et al.2014, ApJ, 792, 128
McMillan P. J., arXiv: 1102.4340v1
Melioli C., Dal Pino E. M. G., Geraissate F. G., arXive:1301.5005v1
Mignone A., Bodo G., Massaglia S., Matsakos T., Tesileanu O., Zanni C., Ferrari A., 2007, ApJSS, 170, 228
Miyamoto M., Nagai R., 1975, PASJ, 27, 533
Mo H. J., Mao S., White S. D. M., 1998, MNRAS, 297, 319-336
Murray, N., Quataert, E., Thompson, T. A. 2005, ApJ, 618, 569
Nath, B. B., Trentham, N. 1997, MNRAS, 291, 505
Nath, B. B., Shchekinov, Y. 2013, ApJL, 777, 12
Newman, S. F., Genzel, R., Förster-Schreiber, N. M., Shapiro Griffin K., Mancini M., Lilly, S. J., Renzini, A., Bouché, N. et al.2012, ApJ, 761, 43
Navarro J. F., Frenk C. S., White S. D. M., 1997, ApJ, 490, 493
Oppenheimer, B. D., Dave, R., 2006, MNRAS, 373, 1265
Oppenheimer, B. D., Dave, R., Keres, D., Fardal, M., Katz, N., Kollmeier, J. A., Weinberg, H., 2010, MNRAS, 406, 2325
Roy A., Nath B. B., Sharma P., Shchekinov Y., 2013, 434, 3572
Rupke, D. S., Veilleux, S., 2013, ApJ, 768, 75
Sembach, K. R., Wakker, B. P., Savage, B. D., Richter, P., Meade, M., Shull, J. M., Jenkins, E.B., Sonneborn, G., Moos, H. W., 2002, arxiv: 0207562v1
Sharma, P., McCourt, M., Parrish, I. J., Quataert, E., 2012, MNRAS, 427, 1219
Sharma M., Nath B., 2013, ApJ, 763, 17
Sharma, M., Nath B., Chattopadhyay I., Shchekinov Y., arXiv: 1306.4362v1
Sharma, P., Roy, A., Nath, B. B., Shchekinov Y., 2014, arXiv 1402.6695
Shopbell, P. L., Bald-Hawthorn, J., 1998, ApJ, 493, 129
Silich, S., Tenorio-Tagle, G., 2001, ApJ, 552, 91
Snowden, S. L. et al.1995, ApJ, 454, 643
Springel, V., Hernquist, L., 2003, MNRAS, 339, 289
Strickland D. K. and Stevens I. R., 2000, MNRAS, 314, 511
Strickland, D. K. and Heckman, T. M., 2007, ApJ, 658,258
Smith M. C., Ruchti G. R., Helmi A., Wyse R. F. G. et al., MNRAS, 2007, 379, 755
Suchkov, A. A., Balsara, D. S., Heckman, T. M., Leitherer, C., 1994, ApJ, 430, 511
Suchkov, A. A., Berman, V. G., Heckman, T. M., Balsara, D. S., 1996, ApJ, 463, 528
Sutherland R. S., Dopita M. A., 1993, ApJSS, 88, 253
Swaters R. A., Sancisi R. and Van der Hulst J. M., 1997, ApJ, 491, 140
Tegmark, M., Silk, J. 1993, ApJ, 417, 54
Tumlinson, J, Thom, C., Werk, J. et al.2011, Science, 334, 948
Vasiliev E. O., Nath B. B., Bondarev R., Shchekinov Y., arXiv: 1401.5070v1
Weaver R., McCray R., Castor J., Shapiro P., Moore R., 1977, ApJ, 218, 377
Weinmann, S. M. et al.2012, MNRAS, 426, 2797

APPENDIX A: ROTATION CURVE AND GRAVITATIONAL ACCELERATION

For the mass model of the galaxy, we take $M_{\rm disk} = 5 \times 10^{10} {\rm M}_{\odot}$, $a = 4.0$ kpc, $b = 0.4$ kpc (Smith et al. 2007), $c = 12.0$ (Maccio et al. 2007) , $d = 6.0$ kpc (the flattening length) and $M_{\rm vir} = 10^{12} {\rm M}_{\odot}$, which gives us $r_{\rm vir} = 258$ kpc and $r_s = 21.5$ kpc. We note that Smith et al. (2007) used a rotation velocity $\simeq 220$ km s^{-1} with $c = 24$, and our assumption of $c = 12$ decreases the rotation velocity by 15%, which we consider to be negligible. The rotation curve can be found from the equation

$$\frac{v_T^2}{R} = \left[\frac{\partial \Phi}{\partial R}\right]_{z=0} = \left[\frac{\partial}{\partial R}(\Phi_{\rm DM} + \Phi_{\rm MN})\right]_{z=0} \quad \text{(A1)}$$

which gives (in units of 10^{14} (cm s^{-1})^2)

$$v_T^2 = -\frac{12.3\, R^2}{(d^2+R^2)\left(1+\frac{\sqrt{d^2+R^2}}{r_s}\right)} + \frac{21.5\, R^2}{\left(R^2+(a+b)^2\right)^{3/2}} + \frac{12.3\, R^2\, r_s \log\left[1+\frac{\sqrt{d^2+R^2}}{r_s}\right]}{(d^2+r^2)^{3/2}} \quad \text{(A2)}$$

The rotation curve is shown in Figure A1.

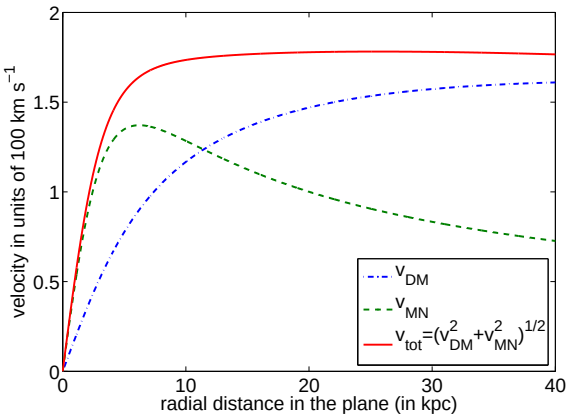

Figure A1. The rotation curve for the galaxy. The plot also shows the contributions from different potential components.

To visualise the gravitational acceleration (g) in the plane and perpendicular to the plane , we plot different components of g in Figure A2. These curves show that the acceleration is not constant in the central region of the Galaxy. This happens because when we go up in z-direction, the total gravitating mass, which can influence a test particle, increases with height. However, at a certain height contribution from the stellar disk becomes maximum, and after that distance, the gravitating mass does not increase much and the acceleration decreases purely due to distance effect.

APPENDIX B: MODIFIED NFW PROFILE

The modified form of NFW profile considered by us is

$$\Phi_{\rm DM} = -\left(\frac{GM_{\rm vir}}{f(c)\, r_s}\right) \frac{\log(1+\sqrt{R^2+z^2+d^2}/r_s)}{\sqrt{R^2+z^2+d^2}/r_s}\,, \quad \text{(B1)}$$

which avoids a singularity at the center. The dark matter density distribution of such a potential can be found using the Poisson's

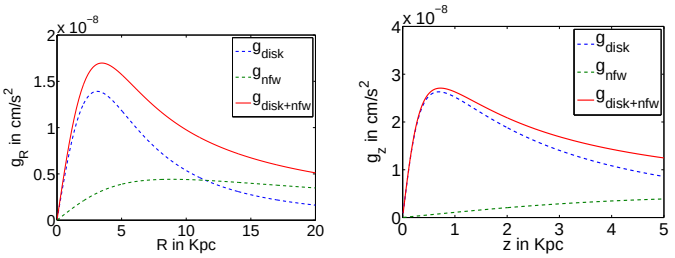

Figure A2. The gravitational acceleration in the plane (left panel) and perpendicular to the plane (right panel).

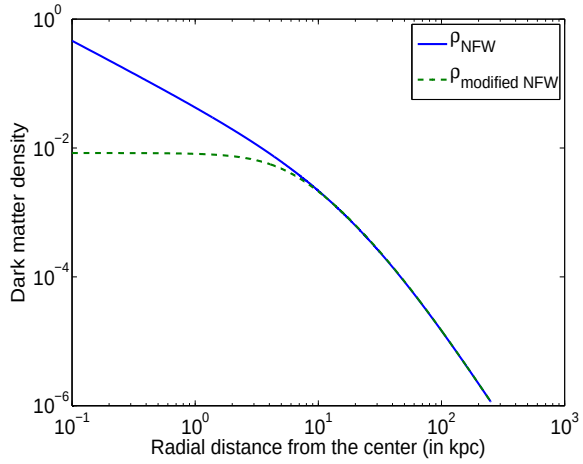

Figure B1. The dark matter density distribution in the Galaxy in units of $\frac{M_{\rm vir}}{4\pi\, f(c)\, r_s}$. The plot uses the parameters for the MW type galaxy mentioned in Table 1.

equation,

$$\rho_{\rm DM}(r) = \frac{1}{4\pi\, G}\nabla^2\Phi_{\rm DM} = \frac{1}{4\pi G}\frac{1}{r^2}\frac{d}{dr}\left(r^2\frac{d}{dr}\Phi_{\rm DM}\right) \quad \text{(B2)}$$

which gives

$$K\,\rho_{\rm DM}(r) = \frac{3r^2}{(d^2+r^2)^2\left(1+\frac{\sqrt{d^2+r^2}}{r_s}\right)} - \frac{3}{(d^2+r^2)\left(1+\frac{\sqrt{d^2+r^2}}{r_s}\right)} + \frac{r^2}{(d^2+r^2)^{3/2}\left(1+\frac{\sqrt{d^2+r^2}}{r_s}\right)^2 r_s} - \frac{3r^2 r_s\log\left[1+\frac{\sqrt{d^2+r^2}}{r_s}\right]}{(d^2+r^2)^{5/2}} + \frac{3r_s\log\left[1+\frac{\sqrt{d^2+r^2}}{r_s}\right]}{(d^2+r^2)^{3/2}}. \quad \text{(B3)}$$

where, $K = \frac{4\pi\, f(c)\, r_s}{M_{\rm vir}}$. This equation reduces to the standard NFW DM density distribution for $d = 0$. The density distribution of the dark matter can be shown in Figure B1.

APPENDIX C: INITIAL DENSITY SETUP

In steady state, for a rotating fluid, force balance along R and z gives

$$0 = -\frac{\partial\Phi}{\partial R} - \frac{1}{\rho}\frac{\partial p}{\partial R} + \frac{v_{\phi,g}^2}{R} \quad \text{(C1)}$$

$$0 = -\frac{\partial\Phi}{\partial z} - \frac{1}{\rho}\frac{\partial p}{\partial z}. \quad \text{(C2)}$$

Here, we use $v_{\phi,g}(R)$ (gas angular velocity is a function of R only) as the rotational velocity of the gas ($p \neq 0$) compared to $v_{\phi,G} = \sqrt{R\frac{\partial\Phi}{\partial R}}$, which we use for the rotational velocity for a pressure-less test particle at $z = 0$. Eq. C2 can be solved as

$$\frac{kT}{\mu m_p\rho}\frac{\partial\rho}{\partial z} = -\frac{\partial\Phi}{\partial z}$$
$$\log\rho = -\frac{\mu m_p}{kT}\Phi + f_1(R)$$
$$\rho(R,z) = \rho_{0R}(R)\exp\left(-\frac{\mu m_p}{kT}\Phi\right), \quad \text{(C3)}$$

where, $\rho_{0R}(R) = \exp[f_1(R)]$. From Eq. C1, we write,

$$\frac{kT}{\mu m_p\rho}\frac{\partial\rho}{\partial R} = -\frac{\partial\Phi}{\partial R} + \frac{v_{\phi,g}^2}{R}$$
$$\log\rho = -\frac{\mu m_p}{kT}\left(\Phi - \int\frac{v_{\phi,g}^2}{R}dR\right) + f_2(z) \quad \text{(C4)}$$

Eq. C3 then gives

$$-\frac{\mu m_p}{kT}\Phi + \log\rho_{0R} = -\frac{\mu m_p}{kT}\left(\Phi - \int\frac{v_{\phi,g}^2}{R}dR\right) + f_2(z),$$
$$\rho_{0R}(R) = \exp\left(\frac{\mu m_p}{kT}\int\frac{v_{\phi,g}^2}{R}dR\right)\times\text{constant}. \quad \text{(C5)}$$

Since, ρ_{0R} is only a function of R by definition, $f_2(z)$ must be a constant. Combining equations C3 and C5, we get,

$$\rho(R,z) = \text{constant}\times\exp\left(-\frac{\mu m_p}{kT}\left[\Phi - \int\frac{v_{\phi,g}^2}{R}\,dR\right]\right). \quad \text{(C6)}$$

For simplicity, let us assume that the gas rotation velocity is a fraction of the particle rotation on the plane ($z = 0$), i.e. $v_{\phi,g} = f\,v_{\phi,G}$, where, f is a constant. Then, Eq. C6 can be written as

$$\rho(R,z) = \text{constant}\times\exp\left(-\frac{1}{c_s^2}\left[\Phi(R,z) - f^2\Phi(R,0)\right]\right). \quad \text{(C7)}$$

Here, $c_s = \sqrt{\frac{kT}{\mu m_p}}$ is the isothermal sound speed of the gas. For a non-rotating gas, the equation becomes

$$\rho(R,z) = \text{constant}\times\exp\left(-\frac{1}{c_s^2}\left[\Phi(R,z)\right]\right). \quad \text{(C8)}$$

The constant can be determined by normalising the density.

Several isothermal components can be combined, as we do for a rotating WIM disc and a non-rotating hot halo.